

# Wide sdB binaries. I. Orbital and atmospheric parameters

Francisco Molina<sup>1,2</sup>, Joris Vos<sup>3</sup>, Alexey Bobrick<sup>4,5</sup>, and Maja Vučković<sup>6</sup>

<sup>1</sup> Institut für Physik und Astronomie, Universität Potsdam, Karl-Liebknecht-Str. 24/25, 14476, Golm, Germany

<sup>2</sup> Dpto. Química "Prof. José Carlos Válchez Martín", Facultad de CC Experimentales, Universidad de Huelva, 21007 Huelva, Spain

<sup>3</sup> Astronomical Institute of the Czech Academy of Sciences, CZ-25165, Ondřejov, Czech Republic

<sup>4</sup> School of Physics and Astronomy, Monash University, Clayton, Victoria 3800, Australia

<sup>5</sup> ARC Centre of Excellence for Gravitational Wave Discovery – OzGrav, Australia

<sup>6</sup> Instituto de Física y Astronomía, Universidad de Valparaíso, Gran Bretaña 1111, Playa Ancha, Valparaíso 2360102, Chile

## ABSTRACT

**Context.** Long-period binary systems containing a B-type hot subdwarf (sdB) and a main-sequence (MS) companion are thought to originate from binary interactions involving stable mass transfer from the red giant, the progenitor of the sdB, to the MS companion. However, despite the recent progress in modelling their population, some of their observed properties are not entirely understood. Because determining their orbits requires extended campaigns of high-resolution spectroscopic observations, only a limited number of long-period sdB binaries have been studied with completely determined orbital parameters.

**Aims.** We aim to expand the current sample of long-period sdB binaries with fully determined orbital parameters through the analysis of high-resolution spectroscopic data. In addition, the atmospheric parameters of the cool companions are analysed. Increasing the number of well-characterized systems will provide valuable insights into their formation channels and main characteristics.

**Methods.** A sample of 32 wide binary systems containing sdB stars was selected for the analysis of the radial velocity (RV) curves of both companions. The dataset consisted of high-resolution spectra obtained with the HERMES and UVES spectrographs. The orbital parameters were derived by simultaneously fitting Keplerian orbits to the RVs of the sdB and its companion. The atmospheric parameters of the cool companions were determined using the GSSP code, which analyses the master spectra of the systems with a grid of LTE atmospheric models. An additional sample of wide sdB binaries was built up by cross-matching the Gaia NSS catalogue with catalogues of sdB candidates and spectroscopically confirmed systems reported by Culpan et al. (2022). The outcomes from both samples were compared with existing theoretical models to assess their consistency with current formation and evolutionary scenarios.

**Results.** The complete orbital solution of the 32 wide sdB binaries was obtained. Their Galactic orbits and kinematics parameters were derived. Likewise, we provide the set of atmospheric parameters of the cool companions.

**Key words.** binaries: spectroscopic, Stars: evolution, Stars: mass-loss, subdwarfs

## 1. Introduction

Binary interactions and mass transfer processes lead to the formation of numerous types of post-interaction binaries, including hot subdwarf B stars, which populate the extreme horizontal branch (EHB). These sdB stars are classically described as core-helium-burning objects with a thin hydrogen envelope (approximately  $0.01 M_{\odot}$ ) and a mass near the canonical core-helium-flash value of  $0.47 M_{\odot}$  (Saffer et al. 1994; Brassard et al. 2001; Heber 2009, 2016), although the actual mass range is likely broader (Arancibia-Rojas et al. 2024). They are characterized by high effective temperatures (20,000 to 40,000 K) and surface gravities typically ranging from 5.0 to 6.0 dex. In the classical scenario, an sdB star forms from the progenitor that lost most of its hydrogen envelope near the tip of the red giant branch and ignited the core through a helium flash (RGB, e.g., Heber 2016).

It is now widely accepted that all sdB stars form exclusively through binary interactions (Heber 2016; Pelisoli et al. 2020), as initially suggested by the early work of Mengel et al. (1975). The three main formation channels proposed to date are: the common-envelope (CE) ejection channel (Paczynski 1976; Han et al. 2002), the stable Roche-lobe overflow (RLOF) channel (Han et al. 2000, 2002), and the formation of a single sdB star through the merger of two helium white dwarfs (WD, Webbink 1984).

The RLOF channel can form long-period sdB binaries with orbital periods exceeding 500 days, typically containing main-sequence stars as cool companions (Vos et al. 2020). Observations of such systems have been first reported in the past decade (Østensen & Van Winckel 2012; Deca et al. 2012; Vos et al. 2012). In particular, some observed orbital periods surpassed the predictions of existing binary population synthesis (BPS) models (Han et al. 2002, 2003), highlighting the need for an updated theoretical framework. Subsequently, Chen et al. (2013) proposed an atmospheric RLOF model to explain periods of up to 1600 days.

The most recent modelling showed good agreement with the observed formation rates, orbital periods, mass ratios, and metallicities of the wide composite sdB population (Vos et al. 2020). However, some relevant features of these systems are not entirely explained by the models to date. A notable case is the eccentricity at long orbital periods. The work of Vos et al. (2015) proposed a theoretical framework to address this issue, based on the combination of two eccentricity pumping mechanisms: phase-dependent RLOF and a circumbinary (CB) disc. Despite this, the model falls short in reproducing the observed trend in longer orbital periods and is unable to predict the eccentricity of the systems.

Increasing the number of accurately determined orbital parameters for long-period sdB binaries will help constrain our understanding of their formation, properties, and evolution.

The article is organised as follows. Sect. 2 describes the main characteristics of the wide sdB binary samples used in this work and summarises the observations' information, based on either ground-based data or Gaia. Sect. 3 outlines the determination of the orbital solutions and parameters for both samples. The analysis of the atmospheric parameters of the cool companions in wide sdB systems is presented in Sect. 4. The Sect. 5 provides the information on the Galactic orbits and kinematics derived parameters of the systems. Subsect. 5.2 establishes the main parameter relations and compares the results with the current theoretical models. A discussion has been developed on the possible causes of agreement or disagreement between observations and models. Finally, Sect. 6 summarises the main findings and conclusions of this work.

## 2. Sample and observations

Two different samples of wide sdB binaries are considered in this article. The first one consists of known sdBs that are part of our long-term observing program. Their collection of high-resolution spectra spans more than fifteen years and involves observations from the MERCATOR telescope at the Roque de los Muchachos Observatory (La Palma, Canary Islands, Spain; Gorlova et al. 2013; Vos et al. 2012, 2013, 2017). The program was extended to cover southern targets using the Very Large Telescope at Paranal Observatory (VLT; Atacama Desert, Chile; Vos et al. 2018, 2019).

The second sample consists of wide sdB binaries observed by Gaia (Gaia Collaboration et al. 2023b), for which orbital solutions have been derived from either Radial Velocity Spectrometer (RVS) data or astrometric measurements. The subsequent sections outline the target selection criteria and the observational data for both samples.

### 2.1. Ground-based sample

This sample consists of known wide sdB binaries whose spectral data were obtained with HERMES (High Efficiency and Resolution Mercator Echelle Spectrograph) at the Mercator telescope and with UVES (Ultraviolet and Visual Echelle Spectrograph) at the VLT. The target candidates were selected from a multitude of low- and medium-resolution spectroscopic and photometric surveys, including but not limited to Green et al. (1986); Downes (1986); Kilkenny et al. (1988); Stark & Wade (2003); Rhee et al. (2006); Wade et al. (2006). The first target selection was performed using the original hot subdwarf database compiled by Østensen (2006), which contains more than 2300 stars. The target list was updated when new bright sdB/Os were found in later surveys. The original surveys and their more recent follow-up observing campaigns have been consolidated in the hot subdwarf catalogues of Geier et al. (2017); Geier (2020) and Culpan et al. (2022).

The final targets were selected based on their magnitude. The northern hemisphere targets with a limiting magnitude of 11.5 in the V band were observed with HERMES, while in the southern hemisphere, targets up to V=14 were included, since a larger telescope was used. Binarity was determined based on radial velocity (RV) variations in the data/spectra. HERMES targets were followed for at least 2 years before determining binarity, usually involving more than 10 observations. The UVES targets

were followed over the course of two observing seasons (6-12 months), discarding from the sample those sources not showing significant variation.

HERMES is a high-resolution spectrograph mounted on the 1.2m Mercator Telescope at the Roque de los Muchachos Observatory in La Palma, Spain. It has a spectral resolution of  $R = 85000$ , and covers a spectral range from 377 to 900 nm (Raskin et al. 2011). It is designed for precise spectroscopic studies of stars managed under conditions of high wavelength stability.

There are 10 targets observed with HERMES between 2009 and 2017: 8 sdBs and 2 long-period binaries containing an evolved O-type hot subdwarf (sdO). A detailed discussion of the HERMES observations can be found in Vos et al. (2017) for the sdB binaries and Molina et al. (2022) for the sdO ones, along with technical information regarding the spectrograph capabilities. The HERMES sample was completed, and no new data have been obtained.

UVES is a high-resolution spectrograph installed on the 8.2m VLT at the Paranal Observatory in Chile. UVES is a two-arm cross-dispersed echelle spectrograph, which was used in standard dichroic-2 437+760 mode, covering a wavelength range of 373–499 nm in the BLUE arm and 565–946 nm in the RED arm. The resolutions achieved for each arm, using a slit width of 1 arcsecond, are  $R = 41,000$  and 42,000, respectively. The spectrograph is designed to study the chemical composition, kinematics, and physical conditions of astronomical objects. The complete set of observations by HERMES and UVES is summarized in Table A.1 of the appendix.

So far, the sample of wide hot subdwarf binaries contains 32 systems whose orbits have been fully solved. Their Galactic locations and color-magnitude diagram (CMD) are shown in Fig. 1. The Gaia G absolute magnitude is derived from the Gaia apparent magnitude (g) listed in Gaia DR3 according to:

$$M_G = g + 5 \cdot \log_{10}(\pi/1000 \text{ mas}) + 5 \quad (1)$$

In the CMD, the sample occupies the extended region populated by hot subdwarf binary systems, located in redder colors than the EHB overdensity of single hot subdwarfs. However, one system in the sample is significantly shifted: BD-07 5977. The cool companion of this system was previously studied and reported as a subgiant star (Vos et al. 2017).

### 2.2. Gaia sample

The non-single star catalogue from Gaia DR3 (NSS<sup>1</sup>, Gaia Collaboration et al. 2023a) gathers the sources whose observations are considered as non-constant in one of the three channels of observation capabilities from the Gaia probe: astrometric, spectroscopic, and photometric. This leads to different approaches and binary orbit models to achieve their orbital parameters<sup>2</sup>.

The data release 3 catalogues<sup>3</sup> by Culpan et al. (2022) contain 6 616 hot subdwarfs with spectroscopic confirmation and a further 61 585 hot subdwarf candidates based on Gaia eDR3. They include multi-band photometry and Gaia eDR3 astrometry, as well as classifications based on spectroscopy and colors.

The cross-matching using TOPCAT<sup>4</sup> (Taylor 2005) between both, the NSS and Culpan et al. (2022) catalogues, yields the

<sup>1</sup> <https://cdsarc.cds.unistra.fr/viz-bin/cat/I/357>

<sup>2</sup> [https://gea.esac.esa.int/archive/documentation/GDR3/Data\\_analysis/chap\\_cu4nss/](https://gea.esac.esa.int/archive/documentation/GDR3/Data_analysis/chap_cu4nss/)

<sup>3</sup> <https://cdsarc.u-strasbg.fr/viz-bin/cat/J/A+A/662/A40>

<sup>4</sup> <https://www.star.bris.ac.uk/~mbt/topcat/>

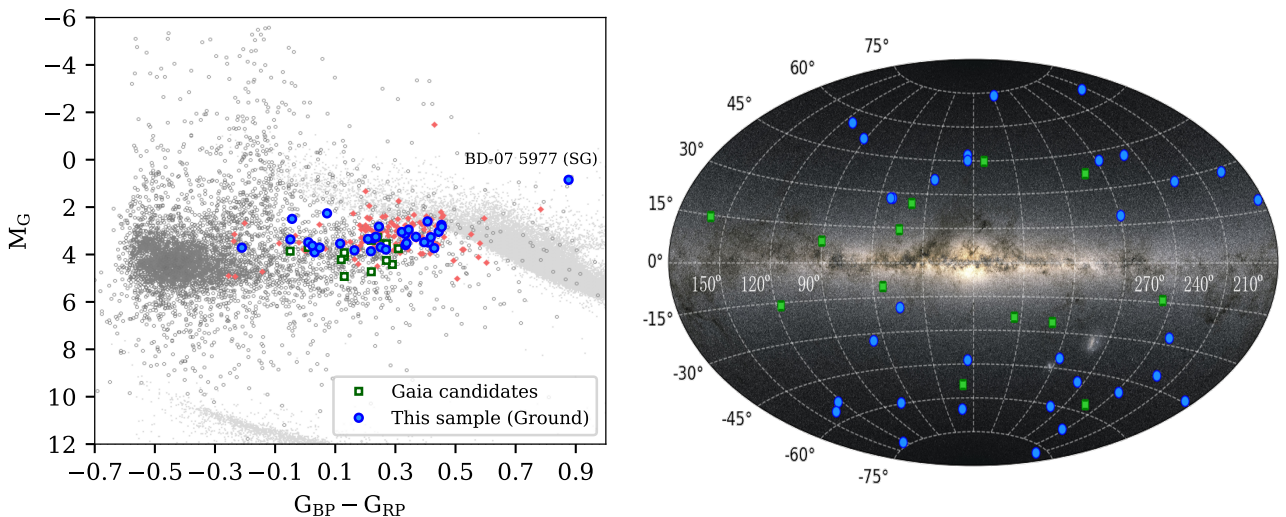


**Fig. 1.** *Left:* The color-magnitude diagram (CMD) presented by [Pelisoli et al. \(2020\)](#) for their composite hot subdwarf sample is shown as dimmed red diamonds, representing systems whose light curves and rotation periods were studied by the authors. We have included the wide hot sdB binary Ground-based sample with fully solved orbital parameters as blue-filled circles. The Gaia-based sample is shown as green-filled squares. Interstellar extinctions for both, Ground- and Gaia-based samples, are not corrected. Stars catalogued by [Geier \(2020\)](#) as hot subdwarfs are represented as dark gray open circles. Main-sequence stars and stars in other evolutionary stages within the region by [Lindegren et al. \(sample C, 2018\)](#) are shown as pale gray dots.

*Right:* An Aitoff projection displaying the Galactic coordinates of the wide hot sdB sample. Galactic longitude increases from the centre toward the left, with increments of 30° per tick. Same color-coded wide sdB systems.

coincidence of 13 sources. Fundamental data of the sources and their observations are listed in Table A.1 of the appendix, along with the wide sdB binary systems. Likewise, their CMDs are shown in Fig. 1 (left panel), along with their Galactic coordinates (right panel).

### 3. Orbital parameters

#### 3.1. Radial velocities

The radial velocities of the cool companion can be determined using cross-correlation (CC). The wavelength intervals used avoid telluric lines and those from the hot companion. They represent a good compromise between the high signal-to-noise ratio (SNR) and the low flux contribution of the hot component. Then, the lines of the cool companion within these intervals are cross-correlated against a high-resolution synthetic template with atmospheric parameters of a similar photometric class to the companion. Before the CC, the synthetic spectrum is convolved to reproduce the line broadening profile of the cool companion star due to the rotational velocity.

The masks utilised for the HERMES spectra are provided by its `hermesVR` pipeline<sup>5</sup>. Meanwhile, for UVES spectra, Kurucz LTE synthetic templates were used ([Kurucz 1979](#)).

The RV error intervals are obtained by performing a Monte Carlo (MC) simulation for each spectrum. Firstly, Gaussian noise is added to the spectrum, based on the continuum noise level in the used wavelength ranges. Then, the synthetic spectrum is used in a new cross-correlation, and the final error is calculated from the standard deviation of the RV results from 500 simulations.

The hot sdB stars pose a greater challenge for determining their RVs due to the limited number of available lines. In many

**Table 1.** Orbital parameters from Gaia-based solutions (NSS) for the wide hot subdwarfs Gaia candidates: orbital periods (P) and eccentricity (e), including their standard errors ( $\sigma$ ). The last field (NSS sol.) accounts for the data Gaia channel and approach from which they were determined. See text in Sect. 2.2 and especially 3.3 for further details.

System	Gaia DR3	P(d)	$\sigma_P(d)$	e	$\sigma_e$	NSS sol.
392046852459641472	884	$\pm 25$	0.497	$\pm 0.090$	Orbital	
4850445797329363328	913	$\pm 80$	0.233	$\pm 0.149$	SB1	
972725503164737152	854	$\pm 32$	0.269	$\pm 0.098$	Orbital	
5579436712515286016	751	$\pm 8$	0.022	$\pm 0.054$	Orbital	
3540092300847749760	617	$\pm 5$	0.087	$\pm 0.068$	Orbital	
6335746093599431296	718	$\pm 41$	0.360	$\pm 0.234$	Orbital	
4550114402362108416	821	$\pm 43$	0.152	$\pm 0.040$	Orbital	
6359368722966483840	740	$\pm 16$	0.231	$\pm 0.080$	Orbital	
4522995326025050496	978	$\pm 188$	0.151	$\pm 0.183$	Orbital	
6631822855308840320	634	$\pm 14$	0.425	$\pm 0.145$	Orbital	
1806581377789928448	847	$\pm 57$	0.207	$\pm 0.059$	Orbital	
2183496162809214464	1138	$\pm 256$	0.067	$\pm 0.131$	Orbital	
6587335519633433472	828	$\pm 29$	0.292	$\pm 0.067$	Orbital	

cases, only the not blended  $\text{He I } \lambda 5876 \text{ \AA}$  line can be used. However, some systems show a few sharp metal lines originating from the sdB companion. If that is the case, the intervals containing those lines are used.

For the hot sdB stars, we employed a custom high-resolution template spectrum. The templates were generated using the

<sup>5</sup> <http://hermes-as.oma.be/manuals/cookbook5.0.pdf>

XTGRID code (Németh et al. 2012; Nemeth 2019). The code uses a wavelength space direct spectral decomposition (Simon & Sturm 1994) to produce synthetic composite spectra through a linear combination of non-LTE (TLUSTY, Hubeny & Lanz 2017) and LTE (ATLAS, Bohlin et al. 2017) atmosphere models. The process involves an iterative fitting routine to the observed spectrum to determine the main parameters of both the hot and cool companions. For obtaining basic templates efficiently and without being time-consuming, initial rough fits to the observed spectra are used as templates for cross-correlation. This approach works, as for the CC, the exact line shape is less important than the presence of the respective lines. The RV error intervals are determined using the MC simulations as described above.

In Table B.1 of the appendix, we indicate the intervals and/or the specific lines used for the CC of the MS and sdB companions.

### 3.2. Keplerian fits and orbital parameters

The orbital parameters were obtained by simultaneously fitting Keplerian orbits to RVs of the companions (Hilditch 2001) with eight free parameters: orbital period ( $P$ ), time of periastron ( $T_0$ ), eccentricity ( $e$ ), angle of periastron ( $\omega$ ), two semi-amplitudes ( $K_1$  and  $K_2$ ) and two systemic velocities ( $\gamma_1$  and  $\gamma_2$ ). The systemic velocities of both components are considered as separate parameters, as the difference in the surface gravity between the components can cause a line-shift (gravitational redshift, see e.g. Vos et al. 2012, 2013).

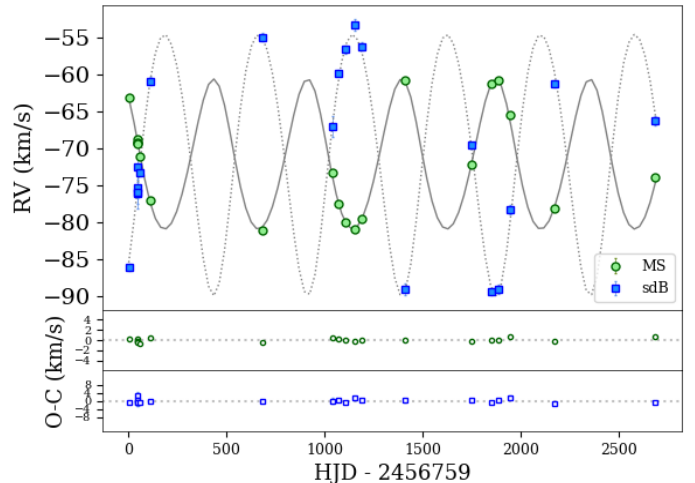
The error intervals on the orbital parameters are calculated using an MC approach, where in each iteration, each single RV measurement is randomly sampled using a normal distribution centred on its best value and a standard deviation equal to its standard error. The final orbital parameters are the mean values of 1000 iterations, while their standard deviations are used as error intervals.

Fig. 2 shows an example of RVs and the simultaneously Keplerian orbits fitted to the companions of the PG1514+034 system. Table B.2 of the appendix presents the orbital parameters obtained from the corresponding solutions for the sample of wide sdB binaries.

### 3.3. Gaia-based orbital solutions

The orbital periods and eccentricities of the wide sdB systems whose orbital solutions were determined by Gaia are shown in Table 1. The data are obtained from the astrometric and photometric channels of Gaia. Gaia orbital solutions of the sample, but for one system, are provided by the model for an astrometric binary source compatible with Campbell orbital elements (Halbwachs et al. 2023). The so-called elements involve the semi-major axis of the orbit described by the photocentre,  $a_0$ , the inclination of the orbital plane with respect to the sky,  $i$ , the position angle of the ascending node,  $\Omega$ , and the periastron longitude measured from the ascending node,  $\omega$ . The measurement of the position of the photocentre relative to the barycentre of the system is related to these elements by a completely nonlinear relationship. The solutions of these elements are obtained by applying the formulas provided by Binnendijk (1960) or Halbwachs et al. (2023).

The  $RA$  and  $Dec$  coordinates and parallaxes (distances) of the Ground-based sample are provided from Gaia DR3. In contrast, for the Gaia sample, the solutions are from the NSS, since they are expected to supersede the original ones in Gaia DR3 (Gaia Collaboration et al. 2023a). Hence, they are used in Table



**Fig. 2.** Radial velocity curves and residuals for PG1514+034. The RVs of the cool companion are plotted as green-filled circles, while those of the sdB companion are shown as blue-filled squares. RV error bars ( $1\sigma$ ), obtained through MC simulations, are included. The best-fit Keplerian orbits, simultaneously fitted for both the MS and sdB companions, are represented by a solid line for the cool companion and a dotted line for the hot one.

1. A detailed description of this solution approach and its constraints is included in the documentation provided on the Gaia-ESA Web<sup>6</sup>.

Orbital parameters for the Gaia DR3 system 4850445797329363328 are derived from its single-lined spectroscopic data (SB1) from the Gaia spectroscopic channel. Following methodology similar to that described in the previous subsection in relation to the SB2 spectra of the wide sdB sample, RVs are fitted using a Keplerian orbit to determine the key orbital parameters of the observed component (Gosset et al. 2024): orbital period ( $P$ ), time of periastron passage ( $T_0$ ), eccentricity ( $e$ ), argument of periastron ( $\omega$ ), RV semi-amplitude ( $K$ ), and systemic radial velocity ( $\gamma$ ). The RV curve is fitted using a general Keplerian function via a least-squares optimization procedure. The quality of the fit is assessed using the reduced chi-squared ( $\chi^2$ ) statistic. A detailed description of the fitting process in SB1 and its constraints is available in the Gaia-ESA documentation<sup>7</sup>.

## 4. Atmospheric parameters of the cool companions

We studied the composite master spectra of the cool companion stars to derive their atmospheric parameters. They were created by shifting the spectra from single observations to the rest velocities of the cool star lines. Then, they were merged, producing a master spectrum with an improved SNR compared to the individual observations. For the analysis of the atmospheric parameters, we used the redward wavelength interval of 6000–6260 Å as a compromise between a high SNR and the contribution of the cool companion. The interval was trimmed and normalized using a polynomial fit to manually selected continuum points.

<sup>6</sup> [https://gea.esac.esa.int/archive/documentation/GDR3/Data\\_analysis/chap\\_cu4nss/sec\\_cu4nss\\_astrobin/ssec\\_cu4nss\\_astrobin\\_orbital.html](https://gea.esac.esa.int/archive/documentation/GDR3/Data_analysis/chap_cu4nss/sec_cu4nss_astrobin/ssec_cu4nss_astrobin_orbital.html)

<sup>7</sup> [https://gea.esac.esa.int/archive/documentation/GDR3/Data\\_analysis/chap\\_cu4nss/sec\\_cu4nss\\_spectroSB1/ssec\\_cu4nss\\_spectroSB1\\_model.html](https://gea.esac.esa.int/archive/documentation/GDR3/Data_analysis/chap_cu4nss/sec_cu4nss_spectroSB1/ssec_cu4nss_spectroSB1_model.html)

Spectroscopic analysis was performed using the Grid Search in Stellar Parameters code (Tkachenko 2015, GSSP). GSSP utilizes a method based on atmospheric models and spectrum synthesis, comparing observations with each theoretical spectrum in the grid. To generate synthetic spectra, this study uses the SynthV LTE-based radiative transfer code (Tsymbal 1996) and a grid of LTE atmosphere models precomputed with the LLMODELS code (Shulyak et al. 2004). Furthermore, it uses an extended grid ( $[M/H] \leq -1.0$  dex) of LTE Kurucz atmosphere models (Kurucz 1979) to work with the most metal-poor systems of the set.

GSSP simultaneously optimizes seven stellar parameters: effective temperature ( $T_{\text{eff}}$ ), metallicity ( $[M/H]$ ), surface gravity ( $\log g$ ), projected rotational velocity ( $v \sin i$ ), macro-turbulent velocity ( $v_{\text{mac}}$ ), micro-turbulent velocity ( $v_{\text{mic}}$ ), and the dilution factor ( $F_{\text{MS}}/F_{\text{Total}}$ ) of the cool companion. A grid of theoretical spectra was built from all possible combinations of these parameters, and GSSP compares them to the observed normalized spectrum. A merit function  $\chi^2$  is used to evaluate the match between the synthetic spectra and the corresponding MS master spectra, identifying the set of best-fit parameters.

The dilution factor was treated as a wavelength-independent parameter within the selected short wavelength interval. Vos et al. (2018) compared this approach with other spectral analysis methods and found that using a fixed dilution factor does not compromise accuracy when applied to short-wavelength ranges.

The values of  $v_{\text{mic}}$  and  $v_{\text{mac}}$  were not freely refined but were fixed in GSSP because the SNR of the master spectra is not high enough to avoid degeneracy and determine these parameters accurately. For these parameters, we adopted the iterative procedure described in Molina et al. (2022), which uses the calibrated relations for  $v_{\text{mic}}$  from Bruntt et al. (2010) and for  $v_{\text{mac}}$  from Doyle et al. (2014). These relations are based on spectroscopic and asteroseismic data of MS field stars.

The initial setup for the parameter search covers a wide range with a large step size to ensure that the global minimum is found while minimizing computational cost. Based on the analysis of this first coarse grid, two consecutive setups with smaller step sizes are implemented. The parameters obtained from each iteration are used to refine the setup for the subsequent search. The outcome of final parameters and their associated errors is determined from the last iteration by fitting a polynomial function to the reduced  $\chi^2$  coefficients. The minimum of the polynomial defines the final parameter value, while the  $1\sigma$  cut-off values provide the error intervals.

Fig. 3 shows the best-fitting GSSP synthetic model for the wavelength range of 6000-6260 Å, applied to the normalized master spectrum of PG1514+034 (also catalogued as EGGR440). Fig. 4 illustrates the derivation of the atmospheric parameter results and their error intervals, in this example,  $v \sin i$  of PG1514+034. The atmospheric parameters derived and their corresponding error intervals for the cool companions of the wide hot sdB binary sample are presented in Table B.3 of the appendix.

## 5. Observed properties

### 5.1. Galactic orbits and kinematics

The Galactic orbits of the wide hot subdwarf binaries are derived using parameters such as their coordinates ( $RA$ ,  $Dec$ ), distance, proper motions in the  $RA$  ( $pmra$ ) and  $Dec$  ( $pmdec$ ) directions, and systemic radial velocity ( $y$ ). As an example, the Fig. 5 illustrates the derived Galactic orbit of the PG1514+034

system, computed using the Python package for Galactic dynamics, GALPY<sup>8</sup>.

The diagram in Fig. 6 shows the  $z$ -component of the angular momentum ( $J_z$ ) against the eccentricity of the Galactic orbits for a calibration sample used by Pauli et al. (2006). The sample of wide hot sdB binaries has been incorporated into this diagram. The calibration sample consists of 291 F- and G-type MS stars, whose Galactic component memberships were previously determined based on both kinematic and chemical criteria (Edvardsson et al. 1993; Fuhrmann 1998, 2004). Three distinct regions (A, B, and C) are identified in the diagram, predominantly populated by thin-disk, thick-disk, and halo stars, respectively. The positions of the wide sdB binary systems within the diagram suggest their probable Galactic population membership. However, the wide sdB binary sample consists of systems in which at least one companion has undergone post-main-sequence evolution. Hence, it is an older and more metal-poor population, which could be associated with also more eccentric Galactic orbits and dynamically hotter kinematics (Wu et al. 2021; Nogueras-Lara et al. 2024).

The eccentricity and  $J_z$  of MCT0146-2651 (also known as SB744) strongly suggest its affiliation with the halo population. Recently studied by Németh et al. (2021), the chemical analysis revealed a low metallicity ( $[M/H] = -1.09$  dex), providing additional support, along with their kinematic parameters, for its likely halo membership.

For the Galactic kinematic study, the velocity components ( $U$ ,  $V$ ,  $W$ ) of the sdB sample were determined using the criteria and calculations outlined in Johnson & Soderblom (1987). These velocities were corrected for solar motion relative to the local standard of rest (LSR) following the criteria of Coşkunoğlu et al. (2011). The results are presented in a Toomre diagram in Fig. 7.

The diagram includes a calibration sample from Chen et al. (2021) for the different Galactic components, incorporating data from the LAMOST MSTO-SG and Gaia DR2 catalogs. The classification of stars into various Galactic components was determined based on kinematic, chemical, and evolutionary considerations, as described in their study. Nevertheless, as generally accepted and indicated, stars with  $V_{\text{tot}} = (U_{\text{LSR}}^2 + V_{\text{LSR}}^2 + W_{\text{LSR}}^2)^{1/2} < 50 \text{ km s}^{-1}$  predominantly, but not exclusively, belong to the thin disk, while those with moderate velocities  $V_{\text{tot}} \approx 70 - 180 \text{ km s}^{-1}$ , are more typically associated with the thick disk (see f.i. Adibekyan et al. 2013; Bensby et al. 2014). Stars linked to the Hercules stream typically meet the criteria of  $V_{\text{LSR}} \approx -50 \pm 9 \text{ km s}^{-1}$  and  $(U_{\text{LSR}}^2 + W_{\text{LSR}}^2)^{1/2} \approx 50 - 70 \text{ km s}^{-1}$  (e.g. Famaey et al. 2005; Bensby et al. 2007). Finally, halo stars are typically characterized by  $V_{\text{tot}} > 220 \text{ km s}^{-1}$  (Bonaca et al. 2017).

Most sdB systems are associated with the thin disk. However, consistent with Fig. 6, some systems are identified as probable candidates for the old thin disk or thick disk: BPS CS 22937, PG2148+095, Feige 87, EC 22540-3324, and JL277. GALEX J053939.1-283329 is a strong candidate for the thick disk, and MCT0146-2651 is identified as a halo system, in agreement with previous findings involving their Galactic orbits.

### 5.2. Parameter relations and comparison with binary evolution models

The determination of the complete set of orbital and cool companion atmospheric parameters for the current sample of wide hot sdB binaries represents an effort that spanned more than a decade of observations. Work is still underway to increase the

<sup>8</sup> <https://docs.galpy.org/>

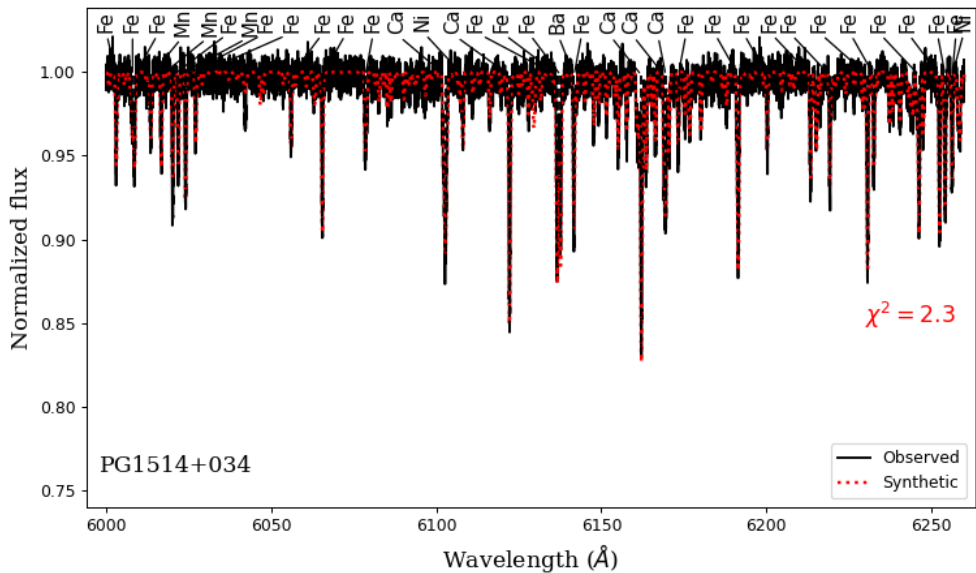


**Fig. 3.** The observed normalized spectrum (black solid line) of PG1514+034 and the best-fitting GSSP model to the cool companion lines (red dotted) for the wavelength range of 6000–6260 Å, used to determine the stellar atmospheric parameters of the cool companion.

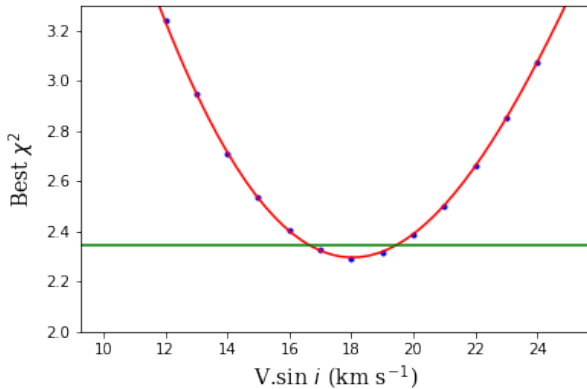


**Fig. 4.** The process of obtaining  $v \sin i$  and its error interval for the cool companion of PG1514+034. The fitting of the polynomial function (in red) to the reduced  $\chi^2$  coefficients (dark blue points) yields the outcome of the atmospheric parameter as the minimum, while the  $1\sigma$  cut-off (green bar) provides its error interval.

number of systems. Nevertheless, the sample obtained so far allows us to establish relationships between orbital and atmospheric parameters and to provide strong constraints on current theoretical frameworks.

The most detailed long-period sdB population study to date, by Vos et al. (2020), used a combination of detailed stellar evolution simulations based on Modules for Experiments in Stellar Astrophysics (MESA, Paxton et al. 2011, 2013, 2015, 2018, 2019), the observationally calibrated Besançon Galactic model (Robin et al. 2003), model for synthetic observations and a standard model of binary interactions. The authors demonstrated that the  $P - q$  distribution of the wide sdBs is partly determined by the metallicity history of the Galaxy and were able to reproduce the observed formation rates, metallicity, period, and mass-ratio distributions. Fig. 8, shows the CMD diagram of Fig. 1, but this time including simulations from Vos et al. (2020).

We note that a significant number of spectroscopic wide sdB binaries occupy a region predicted by the Vos et al. (2020) theoretical model to contain SB1 systems, and are thus offset from

the predictions for composite sdB simulations (left Panel). The simulated sdB systems show  $BP - RP$  colors redder than 0.3 and are dimmer by up to  $\approx 1$  G-band magnitude than the spectroscopic sample. Indeed, a similar conclusion can be drawn for the majority of the composite sdB sample, as reported by Pelisoli et al. (2020), which is included in the CMD. A close analysis of the systems showing colors beyond 0.3, aside from the SG system BD-07 5977 (Vos et al. 2017), indicates that they correspond mostly to those sdB containing cool companions with  $T_{\text{eff}}$  higher than 6000 K (see right Panel of Fig. 8), indicative of Vos et al. (2020) overpredicting the number of the sdBs with the coolest companions. Hence, stars are likely to belong to the F- or earliest G-type spectral class at least. This issue will be addressed in a forthcoming work (Molina et al., paper II, 2026). Observational data from the wide sdB sample will likely help improve the visibility criteria in ongoing and future theoretical work.

The study of the radial velocity curves provides insight into the orbital period distribution of the wide hot sdB sample. The orbital period distribution has been studied since the theoretical work by Vos et al. (2020). Fig. 9 shows the histogram of predicted orbital period distributions from the simulations, based on the visibility criteria, in agreement with the Galactic model.

To construct this histogram, the same method used by Vos et al. (2013) was employed, treating each observation as a normal distribution with the error as the standard deviation. Subsequently, 1,000 orbital periods per system were randomly generated within the uncertainty interval. The resulting 32,000 points (from 32 systems) were binned into intervals of 200 days.

The inclusion of wide sdB Gaia candidates in the orbital period distribution is notably disruptive in the comparison between theoretical and observational distributions. This discrepancy could arise from an observational bias affecting the Gaia sample, since the selection criteria for the Gaia binaries are not identical to those used for the spectroscopic sample. The reported orbital periods tend to cluster in the 700–900-day range, with significant uncertainties in some systems. Alternatively, these Gaia candidates might indicate the existence of a new population of wide sdB systems that has not yet been accounted for by the spectroscopically confirmed sample. Their positions in the above-mentioned CMD diagrams indicate fainter absolute mag-

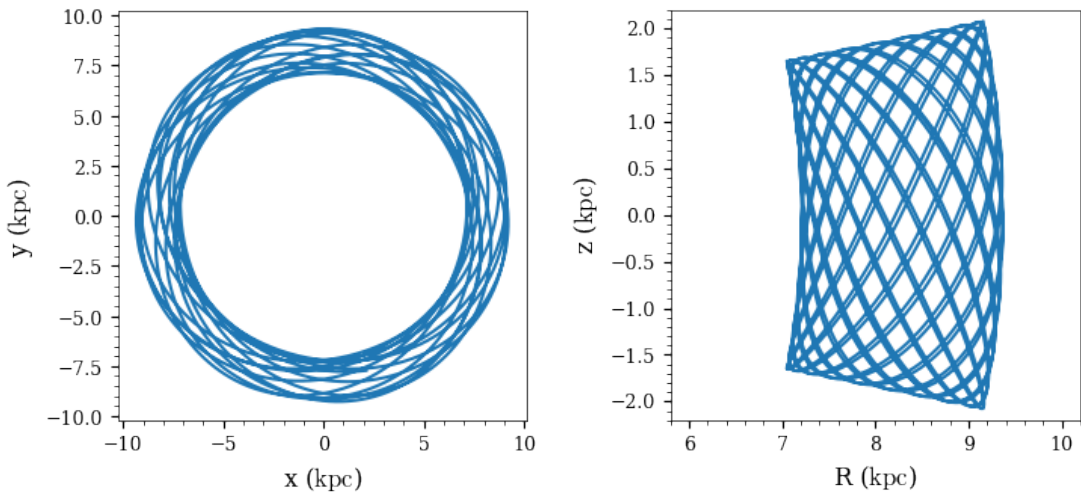


**Fig. 5.** The Galactic orbit of PG1514+034 projected onto the Galactic plane (left) and the vertical Galactic component versus the radius with respect to the Galactic center (right).

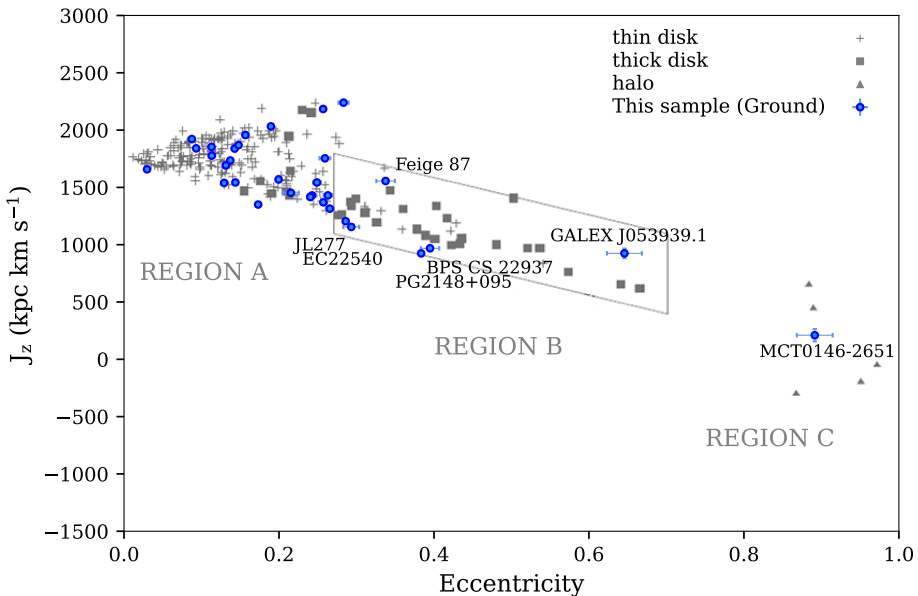


**Fig. 6.**  $J_z$  versus Galactic orbit eccentricity for the calibration sample of main-sequence stars from [Pauli et al. \(2006\)](#). Region A is populated by thin disk stars, region B by thick disk stars, and region C by halo stars. The plot has been adapted to include the Galactic orbit parameters of the wide hot subdwarf sample. The wide sdB systems of the sample, which likely belong to the thick disk or the halo, are labelled. Error bars are included.

mitudes than populations of the current wide sdB or Pelisoli's samples.

The eccentricity of observed binary systems has long challenged theoretical models. Tidal forces are typically expected to lead to orbital circularization. However, observations suggest that eccentricity appears to increase with longer orbital periods (see Fig. 10, Panel A). [Vos et al. \(2015\)](#) proposed a theoretical framework to explain this feature, based on the combination of two eccentricity-pumping mechanisms: phase-dependent RLOF and the formation of a circumbinary disk (CB), which can increase the final eccentricities of the systems. However, while the model successfully accounts for most systems, it is not a population model and does not fully reproduce the observed distribution of systems with the longest and shortest orbital periods.

A closer look at Panel A of Fig. 10, leads us to conclude that, excluding the two systems with unexpectedly long periods (and

the largest eccentricities), the remaining systems do not exhibit such a strong correlation, as initially indicated by the first solved systems more than a decade ago. In our view, this suggests that additional complex factors might be involved in defining the final eccentricity of the systems.

Similarly to the period distribution, the incorporation of the wide sdB Gaia candidates is disruptive in the diagram. This inconsistency may reflect an observational bias between the Gaia and spectroscopic samples, as previously noted regarding the CMD diagram and the orbital period issues. Nonetheless, it should be observed that the Gaia eccentricity measurements are subject to large uncertainties. On the other hand, a similar discrepancy between the eccentricity obtained by Gaia and the ground-based RV measurements of the binary system BD+20 5391 has been observed by [Kurpas et al. \(2025\)](#). The authors

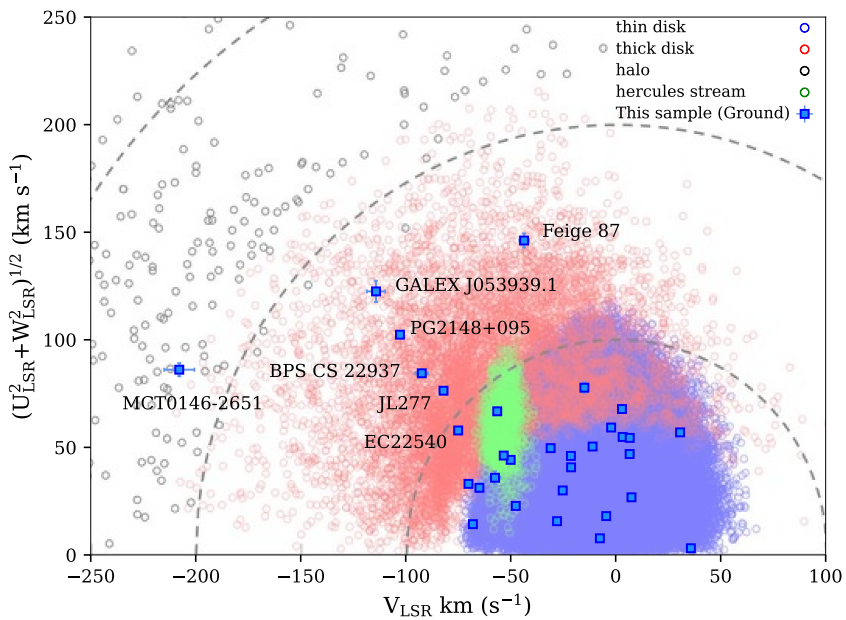


**Fig. 7.** The Toomre diagram of the calibration sample by Chen et al. (2021) for the different Galactic components, attending to kinematics and stellar age criteria (see their paper for thresholds info). The calibration sample contains main-sequence turn-off and subgiants stars from the solar neighbourhood to  $\approx 1500$  pc. The diagram has been adapted (in dimmed colors) to overlap the wide hot subdwarf binary sample. The sdB systems, which are more likely to belong to the thick disk or the halo, are labelled. Included error bars.

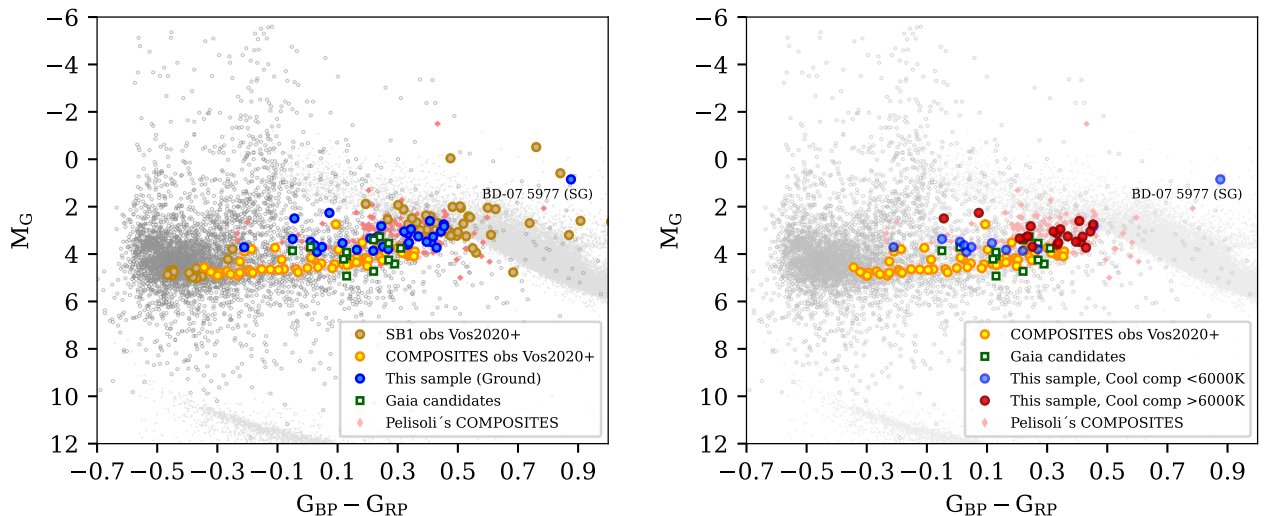


**Fig. 8.** Same CMD diagram than in Fig. 1 but including the simulations by Vos et al. (2020).  
Left panel: Brown filled circles indicating sdB SB1 observable simulations and orange empty ones for observable sdB composites, according to the visibility criteria of the theoretical work.  
Right panel: Only including simulations of observable sdB composites as orange empty circles. The systems in the wide sdB sample with cool companions whose  $T_{\text{eff}}$  is higher than 6000 K are marked with red filled circles.

concluded that Gaia was likely overestimating the eccentricity of the binary system.

Fig. 11 illustrates the agreement between the observations and the theoretical regions predicted by the eccentricity mechanisms from Vos et al. (2015). The Gaia candidate sample further reinforces the apparent discrepancy with the wide sdB sample obtained through spectroscopic methods, but in addition to theoretical models. This might indicate another part of the population detected by Gaia using astrometric methods. However, as previ-

ously noted, their large uncertainties do not allow us to reach strong conclusions.

The formation of a CB disk during the mass loss phase in these systems has not yet been supported by empirical evidence. However, this idea is further supported by the numerous detections and evidence of dusty disks around binary systems, such as eccentric post-AGB binaries (see e.g. Kluska et al. 2022; Oomen et al. 2020, 2018; van Winckel 2017), post-RGB systems (Sarkar & Sahai 2022b; Kamath 2015; Montgomery & Welsh 2012), and post-common-envelope binaries such as the white dwarf binary

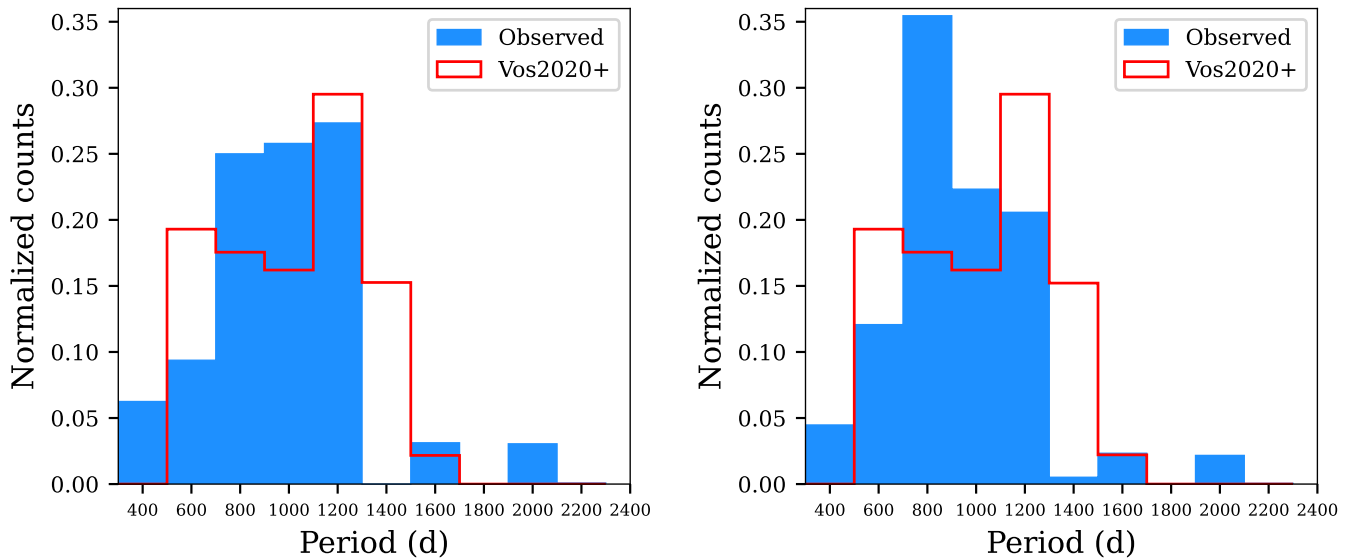


**Fig. 9.** The distribution histogram of orbital periods and the predicted period distributions from the MESA simulations, according to the Galactic model by [Vos et al. \(2020\)](#).

*Left:* Distribution histogram of the wide sdB binary systems sample not including Gaia wide sdB candidates.

*Right:* Distribution histogram including both, the wide sdB binary systems sample and Gaia wide sdB candidates.

NN Serpentis ([Hardy et al. 2016](#)) or the recently published involving a sample of post-common-envelope close hot subdwarf binaries ([Li et al. 2025](#)).

The formation of dust and the associated dusty and debris discs in binary systems has also been addressed from the theoretical point of view (see e.g. [Bermúdez-Bustamante et al. 2024](#); [González-Bolívar et al. 2024](#); [Sarkar & Sahai 2022a](#); [Thebault et al. 2021](#)). Although the gas would be removed early on from a potential CB disk in wide sdB binaries due to photoevaporation, this mechanism is argued to be inefficient for the destruction of relatively small grains ( $\geq 0.01 \mu\text{m}$ ), even in the presence of a strong radiation field ([Nanni et al. 2024](#)). Hence, dust grains could have survived the He core and shell-burning phase. Partially supporting this idea, the recent work by [Li et al. \(2025\)](#) argues for the indirect detection of long-lived circumstellar material around close hot subdwarf binaries as likely remnants of their past common-envelope phase. If remnant material from past CB discs is still linked to wide sdB binaries, contrary to the optically thick discs of Post-AGB or -RGB, a negligible excess in near-IR should be expected (see e.g. transition disks detected in Post-AGB by [Kluska et al. 2022](#)).

Two systems from the wide sdB sample show a slight IR excess in the Longwave-IR WISE W4 band, BD-11 162 and BD-7 5977. They were studied with the ALMA radio telescope ([Molina et al. 2022](#)). However, no remnants of a CB disk were detected. In the case of BD-7 5977, the IR excess may be attributed to the subgiant nature of the cool companion ([Vos et al. 2017](#)). Nevertheless, these results do not rule out the presence of a CB disk in the history of these systems.

According to the previously outlined arguments, the direct detection is complicated, and indirect mechanisms should be developed, as utilised by [Li et al. \(2025\)](#). Their analysis was based on the presence of the Ca II K line, which is linked to the system. This line has been widely used in various studies to trace both transient and stable absorption features from CSM and dusty disks around different types of systems (see e.g. [Vanderbosch et al. 2020](#); [Rebollido et al. 2018](#); [Iglesias et al. 2018](#); [Welsh & Montgomery 2016](#); [Montgomery & Welsh 2012](#)). This topic, re-

garding the current sample of wide sdB with fully solved orbital parameters, will be explored in a forthcoming paper ([Molina et al., in prep., 2026](#)). Confirming the presence of remnant CSM around the systems would suggest that the systems once formed a CB disk.

The correlation between orbital period and mass ratio ( $P - q$ ) in wide sdB binaries was studied by [Vos et al. \(2020\)](#). Their population study concluded that this correlation is strongly linked to the metallicity history of the Galaxy. Furthermore, the model predicts the final  $P - q$  relation in the context of the Galactic membership of the systems. Fig. 10 (Panel B) shows the  $P - q$  observations. In Fig. 12, they are compared to the model of [Vos et al.](#) (see their Fig. 7, 2020). The sdB systems are color-coded based on their probable membership in the Galactic population, which we define using Galactic orbit eccentricity and the boundaries from the calibrated sample by [Pauli et al. \(2006\)](#) in Fig. 6, as well as the kinematic regions in Fig. 7. Systems with Galactic orbital eccentricity less than 0.15 were classified as strong Galactic thin disk candidates. Systems with Galactic orbital eccentricities between 0.15 and 0.45 were classified as a mixture of old thin disk and thick disk (i.e. belonging to either Region A or B). The system GALEX J053939.1-283329 in Region B, with an eccentricity higher than 0.45, consistent with its kinematics, was identified as a strong thick disk candidate. Finally, the system in Region C, MCT0146-2651, given its high Galactic orbital eccentricity and low  $J_z$  (as well as its kinematics and low metallicity), is defined as a strong halo candidate.

Comparing the  $P - q$  relation for the observed ground sample, classified by its Galactic membership, with the simulated sample from [Vos et al. \(2020\)](#) in Fig. 12, we find both good agreement and new open questions. We can see that the bulk of the thin disk lies in the main part of the  $P - q$  relation, overlapping with the simulated sample. The systems with low mass ratio ( $< 0.35$ ) and shorter orbital periods ( $< 1000$  d), PB6355 and HE0430-2457, are consistent with being the extension of the [Vos et al. \(2020\)](#) population towards younger and more massive, non-degenerately-igniting progenitors. The halo candidate system MCT0146-2651 is consistent with the metal-rich end of the

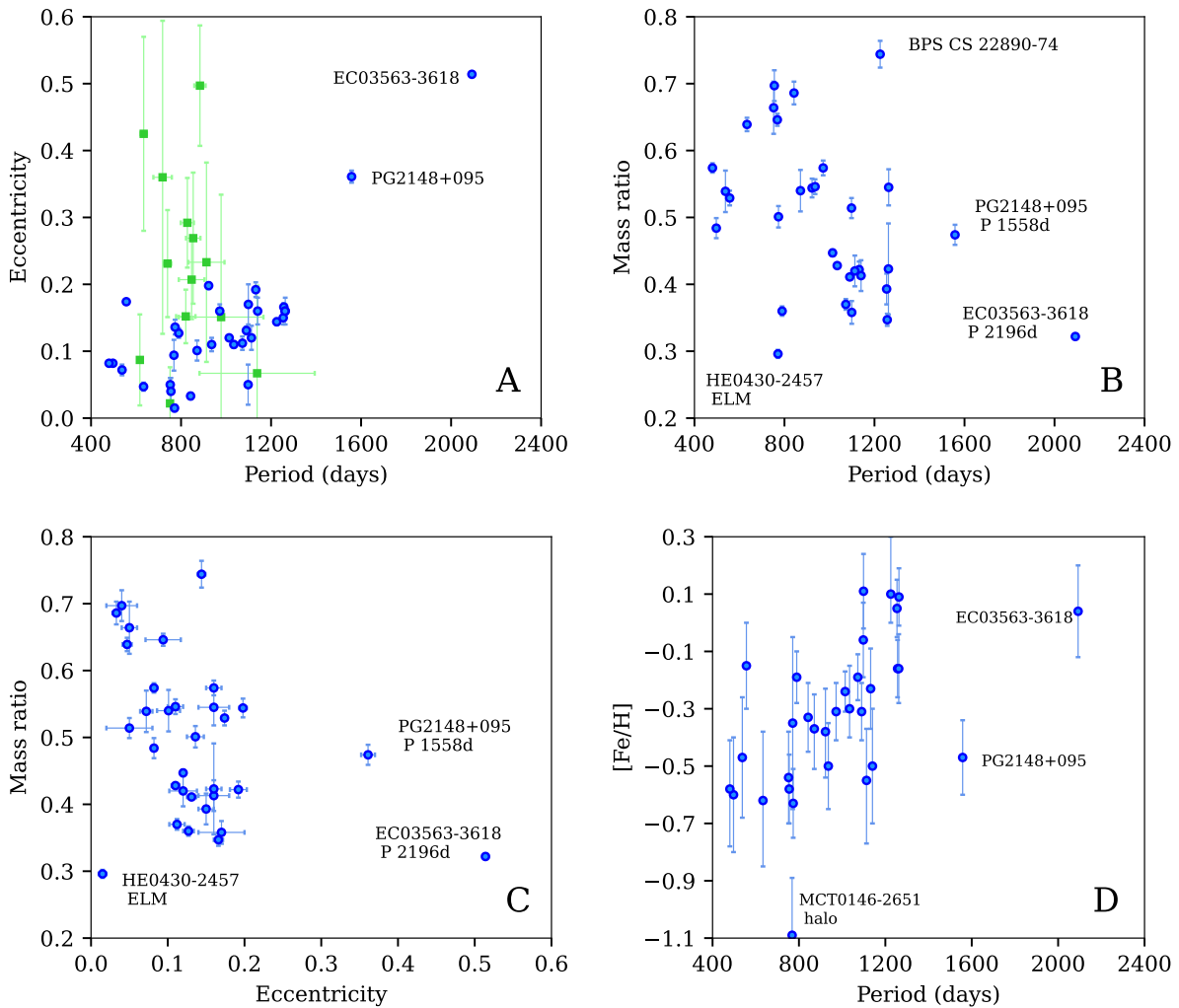


**Fig. 10.** Correlations between orbital parameters derived from the RV curves of the wide sdB binary systems. Error bars are included. *Panel A:* Diagram of the orbital period-eccentricity correlation. *Panel B:* Diagram of the orbital period-mass ratio correlation. *Panel C:* Diagram of the eccentricity-mass ratio correlation. *Panel D:* Diagram of the orbital period-metallicity correlation.

Galactic halo, noting that the Besançon model used in Vos et al. (2020) assumes too narrow a metallicity range for the halo. The strong thick disk candidate GALEX J053939.1 is consistent with the metal-rich part of the Galactic thick disk. Finally, the region with mass ratios of 0.5–0.6 and periods below 750 d, considered to be an unexplained second branch in Vos et al. (2020), can now be seen to mostly consist of old stars, offering a strong clue to its explanation in the population model. Systems PG 2148+095 and especially EC03563-3618 have periods that are very hard to explain by binary models and might be a product of triple stellar evolution (Toonen et al. 2016; Preece et al. 2022). Finally, clustering of binaries in several regions of the  $P - q$  plane, as well as an excess of systems with  $P$  close to 1250 d are new emerging features that need further explanation.

The binary model by Vos et al. (2020) also predicts a theoretical relationship between the final orbital periods and the metallicity of the systems. The Fig. 10 (Panel D) shows the parameters derived from the observations, which are compared with the region predicted by the model. The general agreement is reasonably good. Some outliers are observed, including the two systems with the longest orbital periods (notably, by approximately a factor of two compared to the rest), EC03563-3618 and PG2148+095, as was also the case in the  $P - Ecc$  correlation.

MCT0146-2651 (or SB744), likely a halo member based on its Galactic orbit parameters, kinematics, and metallicity, may also be potentially deviating from the overall relation. At the same time, the second-branch systems in Vos et al. (2020), with orbital periods below 750 d belong to the continuation of the same trend, again suggesting that they are part of the same population.

The sdB companion of MCT0146-2651 exhibits heavy-metal signatures (such as lead and fluorine), which led Németh et al. (2021) to conclude that its formation probably resulted from a merger event in a hierarchical triple system. However, given that the system belongs to the binary population, the most likely explanation is that the heavy-metal signatures result from initial abundances and binary evolution. Additionally, the system EC03563-3618 shows spectral disturbances, suggesting the presence of an additional companion or circumstellar material, possibly an unseen, very long-period cool dwarf. This is a matter for our next study that will outline the observed anomalies in the high-resolution spectra of this system (Molina et al., in prep., 2026).

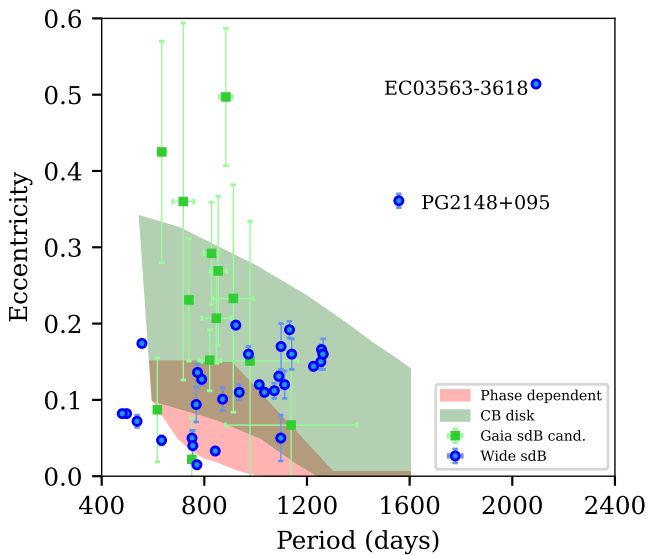


**Fig. 11.** An adapted diagram of the orbital period-eccentricity correlation from Vos et al. (see Fig. 9, 2015). The red-shaded area represents the region explained by RLOF models, while the green-shaded area corresponds to a model incorporating a CB disk formation. The observed systems (blue dots) are plotted with error bars.

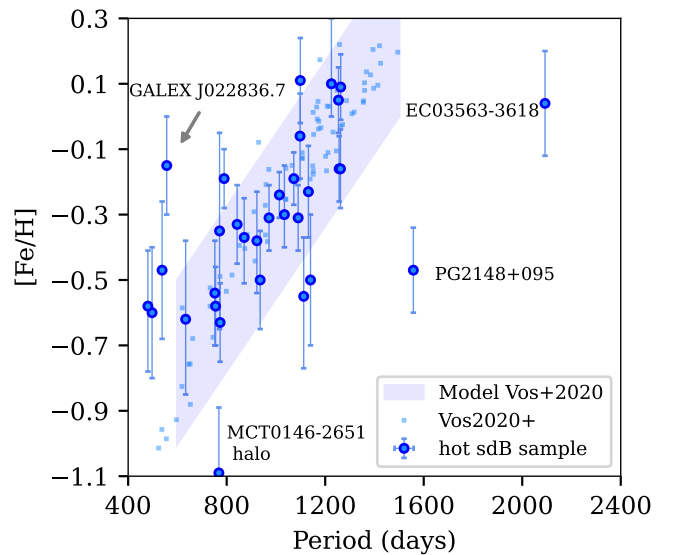


**Fig. 13.** Orbital period versus metallicity for wide sdB binaries. The pale blue region represents the theoretical correlation predicted by Vos et al. (2020), based on a Galactic evolution model combined with a deterministic binary interaction model. Simulations of wide sdB are shown as sky-colored filled squares, wide sdB binaries sample as blue filled circles. Error bars are included.

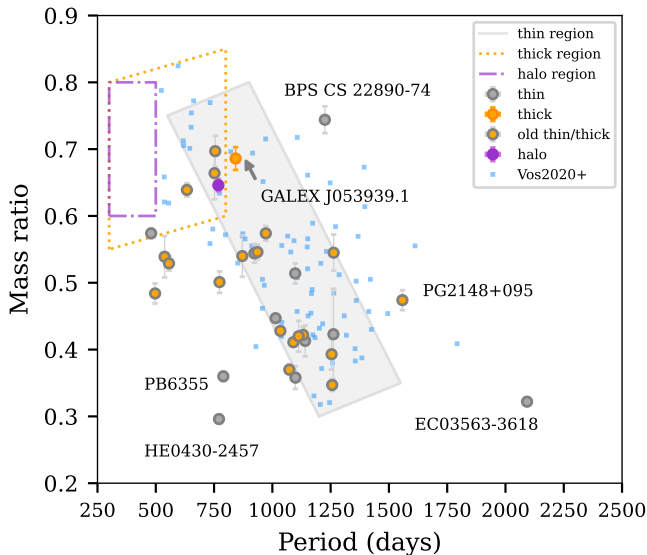


**Fig. 12.** An adapted diagram of the orbital period-mass ratio correlation from Vos et al. (see Fig. 7, 2020). Simulations of wide sdB are shown as sky-colored filled squares. The regions where wide sdBs formed from different Galactic subpopulations are expected to be located are color-coded: thin-disk objects in gray, thick-disk objects in orange, and halo objects in purple. Similarly, the observed systems are color-coded according to their likely Galactic membership. Systems with unclear Galactic membership, thin or thick disk, due to the old population of wide sdB binaries are labelled as old thin/thick. See Sect. 5.1 and 5.2 for a further explanation.

## 6. Conclusions

The orbital parameters of the 32 wide sdB binary systems have been obtained. The data are provided by high-resolution spectra gathered over more than a decade and a half.

Excluding the two outlier systems, EC03563-3618 and PG2148+095, the orbital period distribution of the ground-based wide sdB sample shows good agreement with the Galactic population synthesis model of Vos et al. (2020). These differences become more pronounced when the Gaia-wide sdB sample is included.

Moreover, the Gaia sample shows an anti-correlation between orbital period and eccentricity. However, two factors prevent us from drawing further conclusions: the large uncertainties in the Gaia eccentricity measurements and the narrow orbital period range (700–900 days) where most systems are located. Whether this trend arises from an observational bias or represents a new population of wide sdB systems detected by Gaia remains a matter for further investigation.

Notably, no cross-matching records were obtained from the NSS files for sources compatible with a double-lined spectroscopic binary (SB2) model, even though the NSS files contain more than 5,000 records. This may be significant for the orbital parameters and features of the Gaia sample. Several of the Gaia systems are currently being monitored. Gaia parameters and those derived from comparisons with high-resolution spectroscopy will help clarify this issue.

In contrast, the ground-based sample of wide sdB systems, excluding the two aforementioned outliers, does not show a clear linear relationship between orbital period and eccentricity. This contrasts with earlier studies that suggested otherwise and were based on fewer systems.

In a forthcoming study (Molina et al., paper II, 2026), the mass distributions of the companions in these systems will be derived using a method that combines spectroscopic, photometric, and evolutionary model approaches. The availability of absolute masses will provide other valuable parameters, including absolute separations and orbital inclinations. It will allow one to analyse the rotation periods of the companions and to identify entirely new parameter correlations, providing further strong constraints on binary evolution.

We hope that this comprehensive set of wide sdB binaries will contribute to a better understanding of their formation and their main evolutionary characteristics.

*Acknowledgements.* J.V. acknowledges support from the Grant Agency of the Czech Republic (GAČR 22-34467S). MV acknowledges funding support from the Fondecyt Regular project 1211491. A.B. acknowledges support from the Australian Research Council (ARC) Centre of Excellence for Gravitational Wave Discovery (OzGrav), through project number CE230100016. This work has made use of data from the European Space Agency (ESA) mission *Gaia* (<https://www.cosmos.esa.int/gaia>), processed by the *Gaia* Data Processing and Analysis Consortium (DPAC, <https://www.cosmos.esa.int/web/gaia/dpac/consortium>). Funding for the DPAC has been provided by national institutions, in particular the institutions participating in the *Gaia* Multilateral Agreement. Based on observations collected at the European Southern Observatory under ESO programs 088.D-0364, 093.D-0629, 096.D-0180, 097.D-0110, 098.D-0018, 099.D-0014, 0100.D-0082, 0101.D-0200, 0102.D-0255, 0103.D-0129, 0104.D-0135, 105.20L2.001 and 106.2105.001.

## References

Adibekyan, V. Z., Figueira, P., Santos, N. C., et al. 2013, *A&A*, **554**, A44

Arancibia-Rojas, E., Zorotovic, M., Vučković, M., et al. 2024, *MNRAS*, **527**, 11184

Bensby, T., Feltzing, S., & Oey, M. S. 2014, *A&A*, **562**, A71

Bensby, T., Zenn, A. R., Oey, M. S., & Feltzing, S. 2007, *ApJ*, **663**, L13

Bermúdez-Bustamante, L. C., De Marco, O., Siess, L., et al. 2024, *MNRAS*, **533**, 464

Binnendijk, L. 1960, Properties of double stars; a survey of parallaxes and orbits. (University of Pennsylvania Press)

Bohlin, R. C., Mészáros, S., Fleming, S. W., et al. 2017, *AJ*, **153**, 234

Bonaca, A., Conroy, C., Wetzel, A., Hopkins, P. F., & Kereš, D. 2017, *ApJ*, **845**, 101

Brassard, P., Fontaine, G., Billères, M., et al. 2001, *ApJ*, **563**, 1013

Bruntt, H., Bedding, T. R., Quirion, P. O., et al. 2010, *MNRAS*, **405**, 1907

Chen, D.-C., Xie, J.-W., Zhou, J.-L., et al. 2021, *ApJ*, **909**, 115

Chen, X., Han, Z., Deca, J., & Podsiadlowski, P. 2013, *MNRAS*, **434**, 186

Coşkunoğlu, B., Ak, S., Bilir, S., et al. 2011, *MNRAS*, **412**, 1237

Culpan, R., Geier, S., Reindl, N., et al. 2022, *A&A*, **662**, A40

Deca, J., Marsh, T. R., Østensen, R. H., et al. 2012, *MNRAS*, **421**, 2798

Downes, R. A. 1986, *ApJS*, **61**, 569

Doyle, A. P., Davies, G. R., Smalley, B., Chaplin, W. J., & Elsworth, Y. 2014, *MNRAS*, **444**, 3592

Edvardsson, B., Andersen, J., Gustafsson, B., et al. 1993, *A&A*, **275**, 101

Famaey, B., Jorissen, A., Luri, X., et al. 2005, *A&A*, **430**, 165

Fuhrmann, K. 1998, *A&A*, **338**, 161

Fuhrmann, K. 2004, *Astronomische Nachrichten*, **325**, 3

Gaia Collaboration, Arenou, F., Babusiaux, C., et al. 2023a, *A&A*, **674**, A34

Gaia Collaboration, Vallenari, A., Brown, A. G. A., et al. 2023b, *A&A*, **674**, A1

Geier, S. 2020, *A&A*, **635**, A193

Geier, S., Østensen, R. H., Nemeth, P., et al. 2017, *A&A*, **600**, A50

González-Bolívar, M., De Marco, O., Bermúdez-Bustamante, L. C., Siess, L., & Price, D. J. 2024, *MNRAS*, **527**, 9145

Gorlova, N., Van Winckel, H., Vos, J., et al. 2013, in EAS Publications Series, Vol. 64, EAS Publications Series, ed. K. Pavlovski, A. Tkachenko, & G. Torres, **163**–170

Gosset, E., Damerdji, Y., Morel, T., et al. 2024, *arXiv e-prints*, arXiv:2410.14372

Green, R. F., Schmidt, M., & Liebert, J. 1986, *ApJS*, **61**, 305

Halbwachs, J.-L., Pourbaix, D., Arenou, F., et al. 2023, *A&A*, **674**, A9

Han, Z., Podsiadlowski, P., Maxted, P. F. L., & Marsh, T. R. 2003, *MNRAS*, **341**, 669

Han, Z., Podsiadlowski, P., Maxted, P. F. L., Marsh, T. R., & Ivanova, N. 2002, *MNRAS*, **336**, 449

Han, Z., Tout, C. A., & Eggleton, P. P. 2000, *MNRAS*, **319**, 215

Hardy, A., Schreiber, M. R., Parsons, S. G., et al. 2016, *MNRAS*, **459**, 4518

Heber, U. 2009, *ARA&A*, **47**, 211

Heber, U. 2016, *PASP*, **128**, 082001

Hilditch, R. W. 2001, An Introduction to Close Binary Stars (Cambridge University Press)

Hubeny, I. & Lanz, T. 2017, *arXiv e-prints*, arXiv:1706.01937

Iglesias, D., Bayo, A., Olofsson, J., et al. 2018, *MNRAS*, **480**, 488

Johnson, D. R. H. & Soderblom, D. R. 1987, *AJ*, **93**, 864

Kamath, D. 2015, in EAS Publications Series, Vol. 71-72, EAS Publications Series, **129**–134

Kilkenny, D., Heber, U., & Drilling, J. S. 1988, South African Astronomical Observatory Circular, **12**, 1

Kluska, J., Van Winckel, H., Coppée, Q., et al. 2022, *A&A*, **658**, A36

Kurpas, M., Dorsch, M., Geier, S., et al. 2025, *A&A*, **702**, A200

Kurucz, R. L. 1979, *ApJS*, **40**, 1

Li, J., Wolf, C., Li, J., et al. 2025, *MNRAS*, **537**, 1950

Lindegren, L., Hernández, J., Bombrun, A., et al. 2018, *A&A*, **616**, A2

Mengel, J. G., Norris, J., & Gross, P. G. 1975, in BAAS, Vol. 7, **256**

Molina, F., Vos, J., Nemeth, P., et al. 2022, *A&A*, **658**, A122

Molina et al., in prep., 2026

Molina et al., paper II, 2026

Montgomery, S. L. & Welsh, B. Y. 2012, *PASP*, **124**, 1042

Nanni, A., Cristallo, S., Donevski, D., et al. 2024, *A&A*, **684**, A163

Nemeth, P. 2019, in Astronomical Society of the Pacific Conference Series, Vol. 519, Astronomical Society of the Pacific Conference Series, ed. K. Werner, C. Stehle, T. Rauch, & T. Lanz, **117**

Németh, P., Kawka, A., & Vennes, S. 2012, *MNRAS*, **427**, 2180

Németh, P., Vos, J., Molina, F., & Bastian, A. 2021, *A&A*, **653**, A3

Nogueras-Lara, F., Nieuwmuister, N., Schultheis, M., et al. 2024, *A&A*, **690**, A313

Oomen, G.-M., Pols, O., Van Winckel, H., & Nelemans, G. 2020, *A&A*, **642**, A234

Oomen, G.-M., Van Winckel, H., Pols, O., et al. 2018, *A&A*, **620**, A85

Østensen, R. H. 2006, Baltic Astronomy, **15**, 85

Østensen, R. H. & Van Winckel, H. 2012, in Astronomical Society of the Pacific Conference Series, Vol. 452, Fifth Meeting on Hot Subdwarf Stars and Related Objects, ed. D. Kilkenney, C. S. Jeffery, & C. Koen, **163**

Paczynski, B. 1976, in IAU Symposium, Vol. 73, Structure and Evolution of Close Binary Systems, ed. P. Eggleton, S. Mitton, & J. Whelan, **75**

Pauli, E. M., Napiwotzki, R., Heber, U., Altmann, M., & Odenkirchen, M. 2006, *A&A*, **447**, 173

Paxton, B., Bildsten, L., Dotter, A., et al. 2011, *ApJS*, **192**, 3

Paxton, B., Cantiello, M., Arras, P., et al. 2013, *ApJS*, **208**, 4

Paxton, B., Marchant, P., Schwab, J., et al. 2015, *ApJS*, **220**, 15

Paxton, B., Schwab, J., Bauer, E. B., et al. 2018, *ApJS*, **234**, 34

Paxton, B., Smolec, R., Schwab, J., et al. 2019, *ApJS*, **243**, 10

Pelisoli, I., Vos, J., Geier, S., Schaffenroth, V., & Baran, A. S. 2020, *A&A*, **642**, A180

Preece, H. P., Hamers, A. S., Battich, T., & Rajamuthukumar, A. S. 2022, *MNRAS*, **517**, 2111

Raskin, G., van Winckel, H., Hensberge, H., et al. 2011, *A&A*, **526**, A69

Rebollido, I., Eiroa, C., Montesinos, B., et al. 2018, *A&A*, **614**, A3

Rhee, J., Seibert, M., Østensen, R. H., et al. 2006, Baltic Astronomy, **15**, 77

Robin, A. C., Reylé, C., Derrière, S., & Picaud, S. 2003, *A&A*, **409**, 523

Saffer, R. A., Bergeron, P., Koester, D., & Liebert, J. 1994, *ApJ*, **432**, 351

Sarkar, G. & Sahai, R. 2022a, *ApJ*, **940**, 54

Sarkar, G. & Sahai, R. 2022b, in IAU Symposium, Vol. 366, The Origin of Outflows in Evolved Stars, ed. L. Decin, A. Zijlstra, & C. Gielen, **314**–320

Shulyak, D., Tsymbal, V., Ryabchikova, T., Stütz, C., & Weiss, W. W. 2004, *A&A*, **428**, 993

Simon, K. P. & Sturm, E. 1994, *A&A*, **281**, 286

Stark, M. A. & Wade, R. A. 2003, *AJ*, **126**, 1455

Taylor, M. B. 2005, in Astronomical Society of the Pacific Conference Series, Vol. 347, Astronomical Data Analysis Software and Systems XIV, ed. P. Shopbell, M. Britton, & R. Ebert, **29**

Thebault, P., Kral, Q., & Olofsson, J. 2021, *A&A*, **646**, A173

Tkachenko, A. 2015, *A&A*, **581**, A129

Toonen, S., Hamers, A., & Portegies Zwart, S. 2016, *Computational Astrophysics and Cosmology*, **3**, 6

Tsymbal, V. 1996, in Astronomical Society of the Pacific Conference Series, Vol. 108, M.A.S.S., Model Atmospheres and Spectrum Synthesis, ed. S. J. Adelman, F. Kupka, & W. W. Weiss, **198**

van Winckel, H. 2017, in IAU Symposium, Vol. 323, Planetary Nebulae: Multi-Wavelength Probes of Stellar and Galactic Evolution, ed. X. Liu, L. Stanghellini, & A. Karakas, **231**–234

Vanderbosch, Z., Hermes, J. J., Dennihy, E., et al. 2020, *ApJ*, **897**, 171

Vos, J., Bobrick, A., & Vučković, M. 2020, *A&A*, **641**, A163

Vos, J., Németh, P., Vučković, M., Østensen, R., & Parsons, S. 2018, *MNRAS*, **473**, 693

Vos, J., Østensen, R. H., Degroote, P., et al. 2012, *A&A*, **548**, A6

Vos, J., Østensen, R. H., Marchant, P., & Van Winckel, H. 2015, *A&A*, **579**, A49

Vos, J., Østensen, R. H., Németh, P., et al. 2013, *A&A*, **559**, A54

Vos, J., Østensen, R. H., Vučković, M., & Van Winckel, H. 2017, *A&A*, **605**, A109

Vos, J., Vučković, M., Chen, X., et al. 2019, *MNRAS*, **482**, 4592

Wade, R. A., Stark, M. A., Green, R. F., & Durrell, P. R. 2006, *Baltic Astronomy*, **15**, 81

Webbink, R. F. 1984, *ApJ*, **277**, 355

Welsh, B. Y. & Montgomery, S. 2016, *PASP*, **128**, 064201

Wu, Y., Xiang, M., Chen, Y., et al. 2021, *MNRAS*, **501**, 4917

## Appendix A: Observations, table

**Table A.1.** Summary of the main features of wide hot subdwarf binaries from both, Ground- and Gaia-based sample: ICRS coordinates (degrees, J2000), distances (from parallaxes), used spectrograph/TELESCOPE, number of observations, and photometric band magnitudes and RUWE index provided by Gaia DR3. Observations of Hermes, obtained from specific setups for blue or red interval spectra in different sessions, indicated as b/r, respectively. For the Gaia-based sample, their ground observations counterparts are also indicated.

Systems	Other id	ICRS	ra	dec	dist. (pc)	Spect/TEL	Obs (n)	v (mag)	g (mag)	bp-rp (mag)	RUWE
<b>Ground-based sample</b>											
PG 0048+091		12.86220	9.35914	1254.7	331.2	hermes/MERCATOR	56	14.26	14.18	0.25	1.01
BD-11 162		13.06264	-10.66294	331.2	766.3	ubes/VLT	19	11.18	11.08	0.01	3.69
PB 6355		19.11376	6.05317	459.6	ubes/VLT	19	13.04	12.92	0.41	1.08	
MCT 0146-2651		27.18394	-26.60376	866.5	ubes/VLT	12	12.31	12.22	0.03	2.60	
FAUST 321	SB 744 J01513-7548	27.84755	-75.81085	869.0	ubes/VLT	30	13.03	12.95	0.37	1.11	
JL 277		30.39326	-53.72875	1513.6	ubes/VLT	30	13.09	13.01	0.23	1.44	
GALEX J022836.7-362543	UCAC4 268-002536	37.15355	-36.42932	845.5	ubes/VLT	30	13.54	13.43	0.27	1.67	
EC 03143-5945	J03154-5924	48.87540	-59.56803	986.4	ubes/VLT	26	13.38	13.31	0.21	1.82	
GALEX J033216.7-023302	J03322-0233	53.06977	-2.55056	981.4	ubes/VLT	26	n.a.	12.56	0.41	1.29	
EC 03563-3618	J03582-3609	59.56180	-36.16069	1083.1	ubes/VLT	24	13.60	13.65	0.45	1.29	
HE 0430-2457		68.26602	-24.85548	978.4	ubes/VLT	29	14.12	14.15	0.05	4.52	
GALEX J053939.1-283329	UCAC2 19821041	84.91349	-28.55862	1083.1	ubes/VLT	26	13.89	13.80	0.02	2.15	
BD+34 1543		107.53229	34.41467	194.4	hermes/MERCATOR	30	10.17	10.05	0.33	2.05	
GALEX J081110.8+273420		122.79523	27.57236	701.3	ubes/VLT	17	12.42	12.48	0.23	1.15	
J090001.55+012851.84	SDSS J090001.54+012850.5	135.00646	1.48067	972.8	ubes/VLT	23	n.a.	13.07	0.33	1.00	
GALEX J101703.6-335502	J10170-3355	154.26530	-33.91725	723.6	ubes/VLT	21	12.91	12.82	0.34	1.37	
PG 1018-047		155.29403	-4.93880	808.5	ubes/VLT	21	13.31	13.25	-0.21	3.48	
EC 11031-1348		166.42254	-14.07340	474.5	hermes/MERCATOR	29/15	11.52	11.43	0.44	0.98	
PG 1104+243		166.85899	24.05297	293.2	hermes/MERCATOR	38	11.39	11.20	0.22	2.30	
Feige 80		199.97331	12.06617	564.8	hermes/MERCATOR	67	11.41	11.26	-0.04	1.85	
Feige 87		205.06136	60.87959	446.5	hermes/MERCATOR	33	11.71	11.61	-0.05	3.73	
TYC 3871-835-1	Balloon 82800003	228.90951	56.89549	462.1	hermes/MERCATOR	56/18	11.42	11.37	0.32	1.95	
PG 15154+034	EGGR 440	229.30947	3.17441	1187.1	ubes/VLT	22	13.99	13.91	0.12	1.34	
BPS CS 22890-74	BPS BS 16559-0077	231.01266	1.57266	1023.2	ubes/VLT	15	13.96	13.87	0.16	1.56	
GALEX J162942.0+111838	J16287+1118	247.17493	11.31105	921.1	ubes/VLT	12	13.22	13.09	0.42	1.13	
TYC 2084-448-1	GALEX J173651.2+280635	264.21339	28.10957	392.3	hermes/MERCATOR	30/20	11.40	11.45	0.40	1.31	
BD+29 3070	BD+29 3070	264.58830	29.14658	293.0	hermes/MERCATOR	31	10.45	10.29	0.34	2.43	
GALEX J202216.8+015225		305.56990	1.87341	720.7	ubes/VLT	18	13.43	13.02	0.43	0.98	
BPS CS 22937-0067	BPS CS 228937-67	318.07302	-38.34854	1563.2	ubes/VLT	15	13.91	13.80	0.25	1.00	
PG 2148+095		327.82034	9.78318	1368.2	ubes/VLT	19	13.04	12.94	0.07	1.27	
EC 225540-3324		344.20349	-33.14053	1520.4	ubes/VLT	15	13.86	13.74	0.45	0.96	
BD -07 5977		349.44497	-6.47523	775.3	hermes/MERCATOR	45/18	10.54	10.30	0.88	1.41	
<b>Gaia-based sample</b>											
392046852459641472	UCAC4 683-002060	4.83582	46.55188	1567	n.a.	n.a.	n.a.	14.25	0.24	1.49	
4850445797329363328	CD-44 1028	48.31331	-43.91643	291	n.a.	n.a.	10.72	10.72	0.22	2.08	
97225503164737152	UCAC4 718-043065	90.40099	53.48223	692	n.a.	n.a.	14.09	13.93	0.22	2.93	
5579436712515286016	UCAC4 275-013588	104.34083	-35.19364	441	ubes/VLT	2	13.25	13.15	0.13	5.55	
3540092300847749760	EC 11383-2238	175.21270	-22.91281	834	ubes/VLT	7	13.31	13.15	0.27	1.62	
6335746093599431296	PG 1459-048	225.52675	-4.99398	830	ubes/VLT	9	13.47	13.35	0.31	1.48	
4550114402362108416	GALEX J172748.4+164456	261.95156	16.74908	839	n.a.	n.a.	13.54	13.48	-0.05	2.85	
635936872296643840		270.50901	-83.28525	992	n.a.	n.a.	n.a.	14.06	0.13	1.96	
4522995326025050496	GALEX J182020.1+170933	275.08390	17.15881	1233	n.a.	n.a.	n.a.	14.67	0.12	1.52	
6631822855308840320	GALEX J200739.6+134043	283.26312	-61.43595	1071	n.a.	n.a.	n.a.	14.57	0.29	1.45	
180581377789928448		301.91495	13.67885	1090	n.a.	n.a.	n.a.	14.11	0.13	2.03	
2183496162809214464		307.72960	54.38706	1500	n.a.	n.a.	n.a.	15.13	0.27	2.16	
6587335519633433472	GALEX J220548.0-351939	331.45085	-35.32744	786	ubes/VLT	9	13.25	13.18	0.01	2.42	

## Appendix B: Orbital and Atmospheric Parameters, tables

**Table B.1.** Intervals and/or lines used in the CC with respect to the MS and sdB spectral mask models.

Systems	CC MS intervals (Å)	CC sdB intervals / lines (Å)
PG 0048+091	[3750, 4160] [4160, 4318] [4380, 4620] [4620, 4885] [4885, 4980] [5940, 6270] [6330, 6506]	He I 5875
BD-11 162	[4725, 4820] [4895, 5385] [5440, 5870] [5880, 6270] [6310, 6540]	He II 4686
PB 6355	[4160, 4318] [4380, 4620] [4885, 4968] [5940, 6270] [6320, 6530]	[3920, 3930] [3980, 3990] [4178, 4188] [4250, 4286] [4350, 4365] [4797, 4814]
MCT 0146-2651	[3750, 4160] [4160, 4318] [4380, 4620] [4620, 4885] [4885, 4980] [5700, 5940] [5940, 6270] [6320, 6530]	He I 5875
Faust 321	[4150, 4313] [4520, 4620] [4690, 4815] [6055, 6205] [6380, 6530]	He I 5875
JL 277	[4180, 4300] [4400, 4430] [4485, 4675] [4725, 4825] [4935, 4980] [5910, 6270] [6330, 6510]	[4030, 4080] [4525, 4575] [4625, 4654] [4708, 4718]
GALEX J022836.7-362543	[4885, 4980] [6096, 6180] [6388, 6466]	[3990, 4000] [4413, 4419] [4628, 4632]
EC 03143-5945	[4180, 4300] [4485, 4675] [4725, 4825] [5885, 5960] [6050, 6200] [6380, 6470]	[4035, 4090] [4150, 4250] [4410, 4460] [4580, 4620] [4620, 4680]
GALEX J033216.7-023302	[4117, 4318] [4160, 4318] [4380, 4620] [4885, 4968] [5940, 6270] [6320, 6480]	[3993, 4048] [4235, 4288] [4580, 4620] [4620, 4680]
EC 03563-3618	[4400, 4468] [4475, 4675] [6000, 6260] [6330, 6450]	Triplet Si III 4553 & 4568 & 4574
HE 0430-2457	[6060, 6200] [6387, 6480]	[3993, 4010] [4410, 4460] [4580, 4620] [4620, 4680]
GALEX J053939.1-283329	[4160, 4318] [4380, 4620] [4885, 4968] [5940, 6270]	He I 5875
BD+34 1543	[4780, 6530]	He I 5875
GALEX J081110.8+273420	[4420, 4465] [4485, 4675] [6000, 6260]	He I 4471 & He I 5875
SDSS J090001.54+012850.5	[4160, 4318] [4380, 4620] [4885, 4968] [5940, 6270] [6320, 6530]	He I 5875
GALEX J101703.6-335502	[4160, 4318] [4380, 4620] [4885, 4968]	[4035, 4090] [4220, 4260] [4580, 4620] [4620, 4680]
PG 1018-047	[6095, 6460]	[3910, 3957] [3990, 4082] [4149, 4308] [4364, 4477] [4584, 4721]
EC 11031-1348	[4780, 6530]	He I 5875
PG 1104+243	[4780, 6530]	He I 5875
Feige 80	[4725 4820] [4895, 5385] [5440, 5870] [5880, 6270] [6310, 6540]	He II 4686 & He I 5875
Feige 87	[4780, 6530]	He I 5875
TYC 3871-835-1	[4780, 6530]	He I 5875
PG 1514+034	[4160, 4318] [4380, 4620] [4885, 4968] [5940, 6270] [6320, 6530]	[4548, 4720] & He I 5875
BPS CS 22890-74	[3750, 4160] [4160, 4318] [4380, 4620] [4620, 4885] [5940, 6270] [6320, 6530]	[3990, 4080] [4400, 4450] [4480, 4560] & He I 5875
GALEX J162842.0+111838	[4400, 4468] [4475, 4675] [6000, 6260] [6330, 6450]	He I 5875
GALEX J173651.2+280635	[4780, 6530]	He I 5875
BD+29 3070	[4780, 6530]	He I 5875
GALEX J202216.8+015225	[3750, 4160] [4160, 4318] [4380, 4620] [4620, 4885] [4885, 4980] [5700, 5940] [5940, 6270] [6320, 6530] [6580, 6800]	[4560, 4720] & He I 5875
BPS CS 22937-0067	[4400, 4675] [6000, 6260]	He II 4686
PG 2148+095	[4160, 4318] [4380, 4620] [4620, 4885] [4885, 4980] [5700, 5940] [5940, 6270] [6320, 6530]	He I 5875
EC 22540-3324	[4180, 4300] [4485, 4675] [4725, 4825] [5885, 5960] [6050, 6200] [6380, 6530]	[4035, 4090] [4183, 4188] [4410, 4460] [4580, 4620] [4625, 4634]
BD-07 5977	[4780, 6530]	He I 5875

**Table B.2.** Orbital parameters from the Keplerian orbit solutions of the wide hot subdwarf binary systems.

Systems	P(d)	$\sigma_P(d)$	$T_0$ (d)	$\sigma_{T_0}$ (d)	e	$\sigma_e$	$\omega$	$\sigma_\omega$	$K_{\text{MS}}$ (km s $^{-1}$ )	$K_{\text{sdB}}$ (km s $^{-1}$ )	$\gamma_{\text{MS}}$ (km s $^{-1}$ )	$\gamma_{\text{sdB}}$ (km s $^{-1}$ )	q	$\sigma_q$				
PG 0048+091	538	±1	2457489	±7	0.072	±0.008	0.44	±0.08	6.86	±0.06	12.73	±0.72	-19.81	±0.03	-19.28	±0.36	0.539	±0.031
BD-11 162	497	±1	2454837	±3	0.082	±0.002	0.81	±0.01	8.71	±0.02	18.00	±0.50	3.29	±0.01	4.70	±0.30	0.484	±0.015
PB 6355	790	±1	2458092	±15	0.127	±0.007	3.34	±0.11	5.98	±0.08	16.63	±0.20	-0.66	±0.09	3.24	±0.24	0.360	±0.007
MCT 0146-2651	768	±1	2456080	±4	0.094	±0.023	5.39	±0.04	6.69	±0.02	10.36	±0.14	37.41	±0.03	41.78	±0.14	0.646	±0.009
FAUST 321	1014	±1	2455461	±4	0.120	±0.003	0.83	±0.03	5.84	±0.01	13.08	±0.15	-38.43	±0.01	-37.23	±0.13	0.447	±0.005
JL 277	1090	±1	2455885	±5	0.131	±0.006	0.72	±0.03	6.46	±0.04	15.72	±0.07	102.81	±0.04	104.50	±0.05	0.411	±0.003
GALEX J022836.7-362543	557	±1	2457128	±2	0.174	±0.004	5.00	±0.02	9.42	±0.20	17.82	±0.08	-2.13	±0.12	-1.91	±0.05	0.529	±0.011
EC 03143-5945	1034	±2	2457098	±8	0.110	±0.005	4.84	±0.04	7.27	±0.04	16.97	±0.07	39.91	±0.03	41.55	±0.07	0.428	±0.003
GALEX J033216.7-023302	1257	±2	2457336	±6	0.166	±0.006	3.87	±0.04	6.46	±0.04	18.62	±0.11	27.57	±0.03	29.92	±0.07	0.347	±0.009
EC 03563-3618	2092	±4	2457175	±4	0.514	±0.004	4.84	±0.01	4.52	±0.04	14.03	±0.11	10.00	±0.02	11.99	±0.05	0.322	±0.004
HE 0430-2457	771	±1	2456267	±47	0.015	±0.005	4.08	±0.38	5.44	±0.11	18.38	±0.10	4.62	±0.09	6.25	±0.09	0.296	±0.006
GALEX J053939.1-283329	842	±1	2455647	±17	0.033	±0.005	2.05	±0.12	6.72	±0.03	9.80	±0.24	12.85	±0.03	14.29	±0.18	0.686	±0.017
BD+34 1543	972	±2	2451519	±11	0.160	±0.010	1.58	±0.07	5.91	±0.07	10.31	±0.22	32.10	±0.06	33.12	±0.15	0.574	±0.011
GALEX J081110.8+273420	773	±1	2457409	±6	0.136	±0.011	4.09	±0.05	3.49	±0.03	6.97	±0.21	45.29	±0.02	45.08	±0.16	0.501	±0.016
J090001.55+012851.84	1132	±3	2456847	±1	0.192	±0.011	0.17	±0.03	6.79	±0.16	16.06	±0.22	24.80	±0.09	25.65	±0.11	0.422	±0.012
GALEX J101703.6-335502	1073	±2	2457769	±14	0.112	±0.010	3.57	±0.09	1.92	±0.03	5.19	±0.09	-2.80	±0.01	-1.07	±0.05	0.370	±0.008
PG 1018-047	752	±2	2455193	±16	0.050	±0.010	1.60	±0.20	6.95	±0.40	10.46	±0.09	38.38	±0.06	37.82	±0.19	0.664	±0.039
EC 11031-1348	1099	±6	2456600	±20	0.170	±0.030	3.90	±0.10	5.55	±0.15	15.50	±0.60	-14.75	±0.08	-11.40	±0.30	0.358	±0.017
PG 1104+243	755	±3	2450480	±8	0.040	±0.020	0.70	±0.02	4.42	±0.04	6.34	±0.20	-15.59	±0.06	-13.80	±0.20	0.697	±0.023
Feige 80	1140	±5	2454430	±7	0.160	±0.020	5.96	±0.02	6.20	±0.20	15.00	±0.70	40.21	±0.07	39.90	±0.70	0.413	±0.023
Feige 87	936	±2	2453259	±21	0.110	±0.010	2.92	±0.15	8.19	±0.11	15.01	±0.21	32.98	±0.08	34.32	±0.16	0.546	±0.011
TYC 3871-835-1	1263	±5	2454075	±18	0.160	±0.020	2.83	±0.08	2.31	±0.04	4.24	±0.20	-14.98	±0.02	-13.36	±0.12	0.545	±0.027
PG 1514+034	480	±1	2456741	±3	0.082	±0.004	0.44	±0.04	10.18	±0.03	17.72	±0.20	-71.50	±0.03	-70.93	±0.14	0.574	±0.007
BPS CS 22890-74	1225	±1	2456583	±5	0.144	±0.005	0.01	±0.03	6.19	±0.03	8.32	±0.22	-1.45	±0.02	0.76	±0.12	0.744	±0.020
GALEX J162842.0+111838	871	±1	2457547	±13	0.101	±0.015	6.13	±0.11	4.21	±0.07	7.78	±0.43	-42.69	±0.03	-44.18	±0.22	0.540	±0.031
TYC 2084-448-1	1098	±5	2456054	±58	0.050	±0.030	5.63	±0.33	6.30	±0.10	12.25	±0.30	-15.56	±0.06	-13.30	±0.20	0.514	±0.015
BD+29 3070	1254	±5	2453877	±41	0.150	±0.010	1.60	±0.22	6.53	±0.30	16.60	±0.60	-57.58	±0.36	-56.80	±0.90	0.393	±0.023
GALEX J202216.8+015225	923	±1	2457619	±5	0.198	±0.005	2.67	±0.04	6.18	±0.04	11.35	±0.27	-32.19	±0.04	-31.53	±0.21	0.544	±0.014
BPS CS 22937-0067	1113	±2	2456604	±23	0.120	±0.018	3.68	±0.12	6.40	±0.12	15.23	±0.77	-7.90	±0.07	-9.73	±0.49	0.420	±0.023
PG 2148+095	1558	±3	2457342	±1	0.361	±0.009	5.36	±0.01	7.72	±0.12	16.27	±0.45	-145.66	±0.04	-142.13	±0.24	0.474	±0.015
EC 22540-3324	633	±1	2455993	±21	0.047	±0.006	3.53	±0.22	8.65	±0.11	13.53	±0.13	28.53	±0.09	28.98	±0.11	0.639	±0.010
BD-07 5977	1262	±1	2454971	±4	0.160	±0.010	5.50	±0.10	2.62	±0.01	6.20	±1.00	-8.62	±0.01	-5.50	±0.03	0.423	±0.068

**Table B.3.** Atmospheric parameters from spectroscopic analysis by GSSP of cool companions in the wide hot subdwarf binary systems from both Ground-based and Gaia-based observations when Ground observations are available. The Gaia systems shown are part of an ongoing observation program (116.28ZZ.001). Included  $1\sigma$  error intervals.

Systems	$T_{\text{eff}}$ (K)	[M/H] (dex)	$\log g$ (dex)	$v \sin i$ (km s $^{-1}$ )	Dilution
<b>Ground-based sample</b>					
PG 0048+091	6471 $^{+367}_{-388}$	-0.47 $\pm 0.21$	4.6 $\pm 0.6$	26 $\pm 2$	0.68 $\pm 0.14$
BD-11 162	5630 $^{+230}_{-170}$	-0.6 $\pm 0.20$	4.3 $\pm 0.5$	12 $\pm 1$	0.52 $\pm 0.08$
PB 6355	6516 $\pm 146$	-0.19 $\pm 0.09$	4.5 $\pm 0.1$	57 $\pm 2$	0.85 $\pm 0.07$
MCT 0146-2651	5792 $^{+305}_{-285}$	-1.09 $^{+0.20}_{-0.24}$	4.6 $\pm 0.5$	5 $\pm 2$	0.53 $\pm 0.11$
FAUST 321	6663 $\pm 119$	-0.24 $\pm 0.07$	4.5 $\pm 0.1$	26 $\pm 1$	0.77 $\pm 0.06$
JL 277	6694 $\pm 245$	-0.31 $\pm 0.10$	5.0 $\pm 0.3$	32 $\pm 2$	0.64 $\pm 0.12$
GALEX J022836.7-362543	5330 $\pm 180$	-0.15 $\pm 0.15$	4.5 $\pm 0.2$	90 $\pm 5$	0.30 $\pm 0.05$
EC 03143-5945	6080 $\pm 190$	-0.30 $^{+0.15}_{-0.10}$	4.4 $\pm 0.3$	23 $\pm 1$	0.55 $\pm 0.02$
GALEX J033216.7-023302	7108 $\pm 184$	-0.16 $\pm 0.10$	4.2 $\pm 0.4$	99 $\pm 4$	1.00 $\pm 0.03$
EC 03563-3618	6143 $^{+229}_{-200}$	0.04 $\pm 0.16$	4.4 $\pm 0.5$	29 $\pm 2$	0.90 $\pm 0.14$
HE 0430-2457	4620 $^{+170}_{-200}$	-0.35 $\pm 0.30$	4.5 $\pm 0.5$	30 $\pm 3$	0.20 $\pm 0.05$
GALEX J053939.1-283329	5582 $\pm 163$	-0.33 $\pm 0.12$	4.5 $\pm 0.2$	7 $\pm 1$	0.39 $\pm 0.05$
BD+34 1543	6100 $\pm 150$	-0.31 $\pm 0.10$	4.5 $\pm 0.5$	19 $\pm 1$	0.60 $\pm 0.05$
GALEX J081110.8+273420	7031 $^{+224}_{-286}$	-0.63 $\pm 0.12$	5.0 $\pm 0.3$	10 $\pm 1$	0.72 $\pm 0.12$
J090001.55+012851.84	6604 $^{+292}_{-265}$	-0.23 $\pm 0.14$	4.5 $\pm 0.4$	46 $\pm 3$	0.90 $\pm 0.10$
GALEX J101703.6-335502	6306 $\pm 135$	-0.19 $\pm 0.08$	4.5 $\pm 0.2$	19 $\pm 1$	0.69 $\pm 0.04$
PG 1018-047	4461 $\pm 24$	-0.54 $\pm 0.16$	4.1 $\pm 0.1$	19 $\pm 1$	0.10 $\pm 0.03$
EC 11031-1348	6355 $\pm 257$	0.11 $\pm 0.13$	4.3 $\pm 0.5$	70 $\pm 4$	0.84 $\pm 0.10$
PG 1104+243	5851 $\pm 165$	-0.58 $\pm 0.12$	4.4 $\pm 0.2$	12 $\pm 1$	0.57 $\pm 0.06$
Feige 80	6200 $^{+320}_{-290}$	-0.50 $\pm 0.20$	3.9 $\pm 0.6$	29 $\pm 2$	0.55 $\pm 0.11$
Feige 87	5500 $\pm 230$	-0.50 $\pm 0.15$	4.5 $\pm 0.5$	8 $\pm 1$	0.30 $\pm 0.05$
TYC 3871-835-1	6216 $\pm 196$	0.09 $\pm 0.10$	4.3 $\pm 0.3$	15 $\pm 1$	0.61 $\pm 0.04$
PG 1514+034	5704 $^{+245}_{-214}$	-0.58 $^{+0.17}_{-0.20}$	4.5 $\pm 0.4$	18 $\pm 1$	0.54 $\pm 0.12$
BPS CS 22890-74	5630 $^{+170}_{-220}$	0.10 $^{+0.20}_{-0.10}$	4.5 $\pm 0.2$	7 $\pm 1$	0.45 $\pm 0.05$
GALEX J162842.0+111838	6916 $^{+239}_{-292}$	-0.37 $^{+0.12}_{-0.14}$	4.9 $\pm 0.4$	21 $\pm 1$	0.84 $\pm 0.14$
TYC 2084-448-1	6229 $\pm 229$	-0.06 $\pm 0.13$	4.5 $\pm 0.4$	52 $\pm 3$	0.76 $\pm 0.05$
BD+29 3070	6170 $\pm 200$	0.05 $\pm 0.10$	4.3 $\pm 0.4$	52 $\pm 2$	0.70 $\pm 0.04$
GALEX J202216.8+015225	6449 $^{+265}_{-286}$	-0.38 $^{+0.15}_{-0.16}$	4.7 $\pm 0.4$	34 $\pm 2$	0.80 $\pm 0.14$
BPS CS 22937-0067	7008 $^{+395}_{-465}$	-0.55 $^{+0.18}_{-0.32}$	4.9 $\pm 0.6$	37 $\pm 3$	0.74 $\pm 0.20$
PG 2148+095	6537 $\pm 208$	-0.47 $\pm 0.13$	4.5 $\pm 0.1$	24 $\pm 1$	0.45 $\pm 0.07$
EC 22540-3324	5449 $^{+286}_{-245}$	-0.62 $^{+0.24}_{-0.23}$	4.0 $\pm 0.5$	59 $\pm 3$	0.88 $\pm 0.16$
BD-07 5977	4792 $\pm 98$	-0.16 $\pm 0.12$	3.0 $\pm 0.4$	9 $\pm 1$	0.72 $\pm 0.04$
<b>Available Gaia-based sample (Ground observations)</b>					
EC 11383-2238	5669 $\pm 204$	-0.03 $^{+0.16}_{-0.18}$	4.3 $\pm 0.5$	10 $\pm 1$	0.68 $\pm 0.10$
PG 1459-048	6429 $^{+204}_{-229}$	-0.43 $\pm 0.12$	5.0 $\pm 0.4$	5 $^{+1}_{-2}$	0.62 $\pm 0.08$
GALEX J220548.0-351939	5914 $\pm 294$	-0.57 $^{+0.18}_{-0.20}$	4.7 $\pm 0.5$	2 $\pm 2$	0.43 $\pm 0.06$